**Astronomy & Astrophysics**

# Size and properties of the narrow-line region in Seyfert-2 galaxies from spatially-resolved optical spectroscopy ⋆,⋆⋆,⋆⋆⋆

N. Bennert[1,2], B. Jungwiert[2,3,4], S. Komossa[5], M. Haas[1], and R. Chini[1]

[1] Astronomisches Institut Ruhr-Universität Bochum, Universitätsstrasse 150, 44780 Bochum, Germany
    e-mail: [haas;chini]@astro.rub.de
[2] Institute of Geophysics and Planetary Physics, University of California, Riverside, CA 92521, USA
    e-mail: nicola.bennert@ucr.edu
[3] Astronomical Institute, Academy of Sciences of the Czech Republic, Boční II 1401, 141 31 Prague 4, Czech Republic
    e-mail: bruno@ig.cas.cz
[4] CRAL-Observatoire de Lyon, 9 avenue Charles André, 69561 Saint-Genis-Laval Cedex, France
[5] Max-Planck Institut für extraterrestrische Physik, Giessenbachstrasse 1, 85748 Garching, Germany
    e-mail: skomossa@xra.mpe.mpg.de

**ABSTRACT**

*Context.* While [O III] narrow-band imaging is commonly used to measure the size of the narrow-line regions (NLRs) in active galactic nuclei (AGNs), it can be contaminated by emission from surrounding starbursts. Recently, we have shown that long-slit spectroscopy provides a valuable alternative approach to probe the size in terms of AGN photoionisation. Moreover, several parameters of the NLR can be directly accessed.
*Aims.* We here apply the same methods developed and described for the Seyfert-2 galaxy NGC 1386 to study the NLR of five other Seyfert-2 galaxies by using high-sensitivity spatially-resolved optical spectroscopy obtained at the VLT and the NTT.
*Methods.* We probe the AGN-photoionisation of the NLR and thus, its "real" size using diagnostic line-ratio diagrams. We derive physical properties of the NLR such as reddening, ionisation parameter, electron density, and velocity as a function of distance from the nucleus.
*Results.* For NGC 5643, the diagnostic diagrams unveil a similar transition between line ratios falling in the AGN regime and those typical for H II regions as found for NGC 1386, thus determining the size of the NLR. For the other four objects, all measured line ratios fall in the AGN regime. In almost all cases, both electron density and ionisation parameter decrease with radius. Deviations from this general behaviour (such as a secondary peak) seen in both the ionisation parameter and electron density can be interpreted as signs of shocks from the interaction of a radio jet and the NLR gas. In several objects, the gaseous velocity distribution is characteristic for rotational motion in an (inclined) emission-line disk in the centre. We compare our results to those of NGC 1386 and show that the latter can be considered as prototypical also for this larger sample. We discuss our findings in detail for each object.

*Key words.* galaxies: active – galaxies: nuclei – galaxies: Seyfert

## 1. Introduction

The luminous central engine in active galaxies, most likely an accreting supermassive black hole (BH), ionises the surrounding interstellar medium leading to the broad-line region (BLR) in the inner part and the narrow-line region (NLR) further out. Among the central AGN components, the NLR has the advantage to be directly accessible via imaging and spatially resolved spectroscopy, at least for nearby AGNs.

[O III] $\lambda$5007 Å (hereafter [O III]) narrow-band imaging is commonly used to study the NLRs of active galaxies. However, this emission can be contaminated by contributions from star formation, shock-ionised gas or tidal tails, resulting in an apparent

increase of the NLR. In addition, the measured size depends on the depth of the images: when comparing ground based [O III] images of Seyfert galaxies from Mulchaey et al. (1996) with the HST snapshot survey of Schmitt et al. (2003), the latter reveal, on average, six times smaller NLR sizes, probably due to the 15 to 20 times lower sensitivity. These considerations question the definition of the "NLR size" from [O III] imaging alone.

Spatially resolved long-slit spectroscopy is a valuable alternative approach as it can directly probe the size in terms of AGN photoionisation and discriminate the stellar or shock-ionised contribution. In addition, several physical parameters of the NLR such as reddening, ionisation parameter, electron density, and velocity can be directly accessed and analysed as a function of distance from the nucleus.

In Bennert (2005) and Bennert et al. (2006a) (hereafter Paper I), we describe methods developed to probe the AGN-photoionisation of the NLR and thus, its "real" size as well as to derive physical conditions within the NLR of the nearby Seyfert-2 galaxy NGC 1386: We use the galaxy itself for subtracting the stellar template, applying reddening corrections to fit the stellar template to the spectra of the NLR. From spatially resolved spectral diagnostics, we find a transition between central line

---

**Table 1.** Properties of the sample[a].

|  | IC 5063 | NGC 7212 | ESO 362-G008 | NGC 3281 | NGC 5643 | NGC 1386 |
|---|---|---|---|---|---|---|
| altern. name | ESO 187-G023 | MCG +02-56-011 | MCG -06-12-009 | ESO 375-G055 | ESO 272-G016 | ESO 385–G035 |
| $\alpha$ (J2000) | $20^h52^m02\overset{s}{.}3$ | $22^h07^m01\overset{s}{.}3$ | $05^h11^m09\overset{s}{.}1$ | $10^h31^m52\overset{s}{.}1$ | $14^h32^m40\overset{s}{.}8$ | $03^h36^m46\overset{s}{.}2$ |
| $\delta$ (J2000) | $-57°04'08''$ | $+10°13'52''$ | $-34°23'36''$ | $-34°51'13''$ | $-44°10'29''$ | $-35°59'57''$ |
| $i$. (°)[b] | 51 | 66 | 70 | 66 | 31 | 77 |
| PA (°)[c] | 116 | 42 | 167 | 140 | 128 | 25 |
| $v_{hel}$ (km s$^{-1}$) | 3402±6 | 7984±21 | 4785±24 | 3200±22 | 1199±5 | 868±5 |
| $v_{3k}$ (km s$^{-1}$)[d] | 3276 | 7638 | 4809 | 3523 | 1400 | 774 |
| dist. (Mpc)[e] | 47 | 110 | 67 | 50 | 20 | 11 |
| lin. scale (pc/'')[f] | 220 | 504 | 321 | 236 | 95 | 52 |
| morphology | SA(s)0+: | Sab | Sa | SAB(rs+)a | SAB(rs)c | SB(s)0+ |
| AGN Type | Sy2 | Sy2 | Sy2 | Sy2 | Sy2 | Sy2 |
| $E(B-V)_G$ (mag)[g] | 0.061 | 0.072 | 0.032 | 0.096 | 0.169 | 0.012 |
| $M_B$ (mag) | 12.89 | 14.8 | 13.6 | 12.7 | 10.74 | 12.09 |

[a] Unless stated otherwise, the properties were taken from the NASA/IPAC Extragalactic Database (NED).

[b] Host galaxy inclination (De Vaucouleurs et al. 1991; RC3).

[c] Position angle of host galaxy major axis (RC3); for NGC 5643, it was taken from Morris et al. (1985) as it is not given in RC3.

[d] Velocity relative to the 3K background using the NED velocity calculator.

[e] Distance $D$ in Mpc, using $v_{3K}$ and $H_0 = 71$ km s$^{-1}$ Mpc$^{-1}$.

[f] Linear scale $d$ using distance $D$ and $d = 4.848 \times 10^{-6} \cdot D$.

[g] Foreground Milky Way reddening used for reddening correction (Schlegel et al. 1998).

**Table 2.** Observations of the sample

|  | IC 5063 | NGC 7212 | ESO 362-G008 | NGC 5643 | NGC 3281 | NGC 1386 |
|---|---|---|---|---|---|---|
| telescope | NTT | NTT | NTT | NTT/VLT | VLT | VLT |
| date (beg.) | 15/16-Sep.-04 | 17-Sep.-04 | 14/15/16-Sep.-04 | 21-Apr.-04/25-Feb.-04 | 25-Feb.-04 | 25-Feb.-04 |
| exp. time blue (s)[a] | 6000 | 2732 | 5400 | 3600/1800 | 1800 | 1800 |
| exp. time red (s)[a] | 3600 | 1800 | 5400 | 3600/1800 | 1800 | 1800 |
| seeing | <1'' | <1'' | <1'' | 1''/~2'' | ~1''5 | ~1'' |
| slit width | 1'' | 1'' | 1'' | 0''7/1''3 | 0''7 | 0''7 |
| $FWHM_{instr}$ (km s$^{-1}$) | 250 | 250 | 250 | 90/770 | 460 | 460 |
| PA (deg)[b] | 115 | 170 | 163 | 90/66 | 31 | 5 |
| hel. corr. (km s$^{-1}$)[c] | 0 | −12 | +29 | −9/+11 | −4 | −29 |
| average (pixel)[d] | 3 | 3 | 3 | 3/9 | 7 | 5 |
| scale[e] | 1''1 × 1'' | 1''1 × 1'' | 1''1 × 1'' | 1''1 × 1''/1''8 × 1''3 | 1''4 × 0''7 | 1'' × 0''7 |

[a] Total integration time. At the VLT, the blue and red spectral range were covered in one exposure.

[b] Position angle of the slit.

[c] This heliocentric correction was added to the measured radial velocities.

[d] Number of pixel rows which were averaged.

[e] Formal spatial resolution of final extracted spectra.

ratios falling into the AGN regime and outer ones in the H II-region regime. Applying CLOUDY photoionisation models (Ferland et al. 1998), we show that the observed distinction between H II-like and AGN-like ratios in NGC 1386 represents a true difference in ionisation source and cannot be explained by variations of physical parameters such as ionisation parameter, electron density or metallicity. We interpret it as a real border between the NLR, i.e. the central AGN-photoionised region, and surrounding H II regions. We find that both the electron density and the ionisation parameter decrease with radius. The differences between the reddening distributions determined from the continuum slope and the Balmer decrement argue in favour of dust intrinsic to the NLR clouds with varying column density along the line of sight. The NLR and stellar velocity fields are similar and indicate that the NLR gas is distributed in a disk rather than a sphere.

Here, we apply the same methods to a larger sample of five Seyfert-2 galaxies to probe the size of the NLR. We derive

physical properties such as reddening, ionisation parameter, electron density, and velocity, and discuss their variations with distance from the nucleus. In our discussion, we include the results for NGC 1386 from Paper I. A detailed comparison of our results with literature data is given for each object (Appendix; see also Bennert 2005).

A similar study was carried out for six Seyfert-1 galaxies. The results and the comparison with the Seyfert-2 galaxies presented here will be summarised in Bennert et al. (2006c).

## 2. Observations

The spectra were taken in the wavelength range $\sim\lambda3700$–7000 Å to cover the emission lines suited for specific diagnoses: H$\alpha$ and H$\beta$ (normaliser, reddening indicator); [O II] $\lambda3727$ Å/[O III] $\lambda5007$ Å (sensitive to ionisation parameter); [O III] $\lambda\lambda4363,5007$ Å (temperature sensitive); [O I] $\lambda6300$ Å, [N II] $\lambda6583$ Å, [S II] $\lambda\lambda6716,6731$ Å (AGN
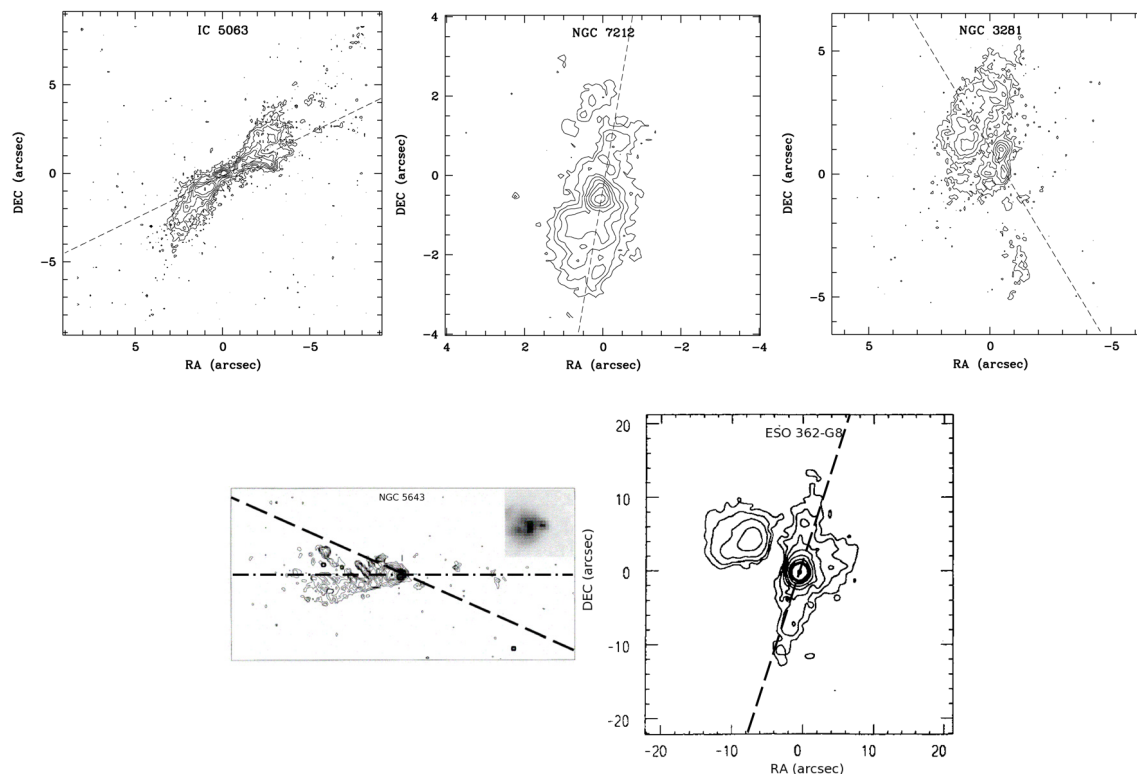
**Fig. 1.** HST [O III] images of the Seyfert-2 galaxies IC 5063, NGC 7212, and NGC 3281 (WF chip: $\sim0\rlap{.}''1$ pix$^{-1}$) taken from Schmitt et al. (2003). Contours start at the $3\sigma$ level above the background (Schmitt et al. 2003, their Table 2) and increase in powers of 2 times $3\sigma$ ($3\sigma \times 2^n$). The HST [O III] image of NGC 5643 was taken from Simpson et al. (1997) and has the dimensions $30'' \times 15''$. The inset shows the central $1'' \times 1''$. The direction of the long slit used in our VLT observations is presented by the long-dashed black line while the PA of the long slit used in the NTT observations by Christian Leipski is indicated by the dashed-dotted black line. The groundbased [O III] image of ESO 362-G008 was taken from Mulchaey et al. (1996). The position of the long slit is shown as dashed line. North is up, east to the left.

classifier); [S II] $\lambda6716\,\text{Å}$/[S II] $\lambda6731\,\text{Å}$ (sensitive to electron density).

Relevant information on the sample and observations is summarised in Tables 1 and 2.

### 2.1. VLT/FORS1

The high signal-to-noise ratio (*S/N*) long-slit spectra of three Seyfert-2 galaxies (NGC 3281, NGC 5643, and NGC 1386) described here were obtained using FORS1[1] attached to the Cassegrain focus of UT1 at the VLT on the 25th of February 2004. Observations were made in the spectral range 3050–8300 Å through the nucleus of each galaxy with exposure times of 1800 s with a typical seeing of $\sim$1–2$''$. The spatial resolution element is $0\rlap{.}''2$ pix$^{-1}$.

The slit width was chosen according to the seeing corresponding to $0\rlap{.}''7$–$1\rlap{.}''3$ on the sky. These slit widths project to a spectral resolution of $\sim$8–14 Å ($\sim$450–770 km s$^{-1}$) as is confirmed by the full-width-at-half-maximum (*FWHM*) of wavelength calibration lines as well as of the [O I] $\lambda5577\,\text{Å}$ night-sky line. The length of the slit used corresponds to $6\rlap{.}'8$ on the sky. The slit was orientated along the position angle (PA) of the maximum extent of the high excitation gas observed in narrow-band images centred on [O III] from Schmitt et al. (2003) in the cases of NGC 3281 and NGC 1386. For NGC 5643, the PA from the HST [O III] image of Simpson et al. (1997) was planned to be used. However, by mistake, the observed PA differ by 24° to the PA of the major [O III] extension (66° instead of 90°).

Fortunately, this galaxy was observed in a different observing run at the NTT at a PA of 90° by Christian Leipski, who kindly provided us with these data (see next section for details). We nevertheless used the high *S/N* VLT data to derive the stellar template of the galaxy itself and apply it to the NTT data.

As UT1 (FORS1) is equipped with an atmospheric dispersion corrector (ADC), there was no need to consider the effects of atmospheric diffraction. The [O III] images with the slit position overlaid are shown in Fig. 1.

### 2.2. NTT/EMMI

High *S/N* long-slit spectra of another three Seyfert-2 galaxies (IC 5063, NGC 7212, and ESO 362-G008) were obtained using EMMI[2] attached to the Nasmyth B focus of the NTT from the 14th to the 17th of September 2004. Medium dispersion spectroscopy was performed in the observing modes REMD[3] and BLMD[4] in the red and blue wavelength range, respectively. The spatial resolution element is $0\rlap{.}''37$ pix$^{-1}$ in the blue and $0\rlap{.}''33$ pix$^{-1}$ in the red. Observations were made in the spectral range 3650–5350 Å (blue) and 4540–7060 Å (red) through the nucleus of each galaxy. All four nights were photometric with a typical seeing of $\sim$0.5–1$''$. Thus, for all objects, a slit width of 1$''$ was chosen. It projects to a spectral resolution of $\sim$4 Å ($\sim$250 km s$^{-1}$ at [O III]) as is confirmed by the *FWHM* of wavelength calibration lines as well as of the

---

[1] FOcal Reducer/low dispersion spectrograph.

[2] ESO Multi-Mode Instrument.

[3] REd Medium Dispersion spectroscopy.

[4] BLue Medium Dispersion spectroscopy.

[O I] $\lambda$5577 Å night-sky line. The slit (5.'5) was orientated along the PA of the maximum extent of the [O III] emission taken from Mulchaey et al. (1996) for ESO 362-G008, and from Schmitt et al. (2003) for IC 5063 and NGC 7212 (Fig. 1).

Additionally, NGC 5643 was observed with EMMI at the NTT in REMD mode (spatial resolution $\sim$0.''33 pix$^{-1}$) on April 21st 2004 by Christian Leipski. The seeing was $\sim$1$''$ and the slit corresponds to 0.''7. NGC 5643 was observed at a low airmass ($<$1.1) with a total integration time of 3600 s in both the blue (4650–5450 Å) and the red wavelength range (6500–7250 Å). While the spectral resolution is high ($\sim$1.5 Å $\simeq$ 90 km s$^{-1}$ at [O III]), the spectral range does not cover the [O II] $\lambda$3727 Å and the [O I] $\lambda$6300 Å lines. Therefore, we can neither derive the ionisation parameter from the ratio [O II]/[O III] nor the second diagnostic diagrams which involves the [O I] line.

At the NTT, no ADC is available. As we aimed to observe along the major extension of the [O III] emission, we could not observe along the parallactic angle. Thus, several precautions were taken: (i) A blue filter was used to centre the objects for observations in the blue wavelength range, and vice versa for the red. (ii) All objects were observed at airmasses smaller than 1.3 so that the atmospheric differential refraction is smaller than the slit width in both the blue and red wavelength range (Filippenko 1982).

## 3. Reduction and analysis

### 3.1. Data reduction

Standard reduction including bias subtraction, flat-field correction, and cosmic-ray rejection was performed using the ESO MIDAS[5] software (version Nov. 99). Night-sky spectra at 1–3$'$ distance on both sides of any notable galaxy emission were interpolated in the region of the galactic spectrum and subtracted in each case.

Wavelength calibration was achieved by rebinning the spectra to a scale of 2.65 Å pix$^{-1}$ for the VLT spectra. For the NTT data, a scale of 1.84 Å pix$^{-1}$ for the blue and 1.58 Å pix$^{-1}$ for the red wavelength range was obtained. For NGC 5643, the spectra taken by Christian Leipski have a higher resolution, corresponding to a scale of 0.4 Å pix$^{-1}$. The curve of Tüg (1997) was used to correct for atmospheric extinction. The spectra were flux calibrated using the standard star CD-32°9927 in case of the VLT data and LTT 7379 for the NTT data (and LTT 3684 for NGC 5643, respectively). Foreground Milky Way reddening was corrected using values from Schlegel et al. (1998), as listed in NED, and the extinction law from Savage & Mathis (1979). Forbidden-line wavelengths were taken from Bowen (1960). Heliocentric corrections as given in Table 2 were added to the observed velocities.

### 3.2. Extraction of spatially resolved spectra

In the spatial direction perpendicular to the dispersion axis, several pixel rows were extracted (see below). Each pixel row corresponds to 1–2$''$ along the slit direction. In the case of the EMMI spectra, the spectra taken with the red chip and its slightly higher spatial resolution (0.''33 pix$^{-1}$ compared to 0.''37 pix$^{-1}$ in the blue) were rebinned to the resolution of the blue chip.

We choose the spectrum with the maximum intensity of the continuum as "photometric centre" ("zero" on the spatial scale).

---

[5] Munich Image Data Analysis System, trade mark of ESO.

**Table 3.** Template subtraction details[a].

| Galaxy | Distance | Size |
|---|---|---|
| IC 5063 | 23$''$ (NW) | 7$''$ |
| ESO 362-G008 | 6$''$ (SE) | 1$''$ |
| NGC 3281 | 11$''$ (SW) | 1.''5 |
| NGC 5643[b] | 26$''$ (SW) | 2$''$ |
| NGC 1386 | 18$''$ (N) | 5$''$ |

[a] The template distance from the nucleus is given with the direction in brackets as well as the size (diameter) of the region that was averaged to obtain the template. The spectra were median-filtered over three pixels to increase the S/N.

[b] Template taken from VLT spectra (PA 66°) due to higher S/N; no reddening correction applied.

It coincides with the highest emission-line fluxes in H$\alpha$ and [O III]. In the following, we also refer to it as "central spectrum". Note that this optical centre needs not to coincide with the position of the AGN, which may be hidden by dust. In the case of the FORS1 spectra, between three and nine pixel rows were averaged according to the seeing to enhance the S/N without losing any spatial information. Table 2 lists detailed information on each galaxy. We averaged 3 pixel rows of all NTT spectra, corresponding to 1.''1. Line intensities and ratios refer to windows of 1 square arcsecond size. On average, we could measure [O III] emission at a S/N $>$ 3 out to $r \sim 13''$ distance from the nucleus, ranging from a spatial coverage of 4$''$ (ESO 362-G008) to 20$''$ (IC 5063), plus extended H II regions in some galaxies (e.g. in NGC 5643 out to 75$''$ ($\sim$7 kpc) from the centre). Line ratios at a S/N $>$ 3 were measured out to an average distance of $r \sim 8''$.

The angular distances were transformed to linear distances at the galaxies (Table 1). As the linear distances are projected distances and depend on the (uncertain) distance to the galaxy, we instead use in our figures the angular scale on the x-axis and give a scale bar as a measure of the corresponding linear scale.

### 3.3. Subtracting the stellar population

As discussed in Paper I, removing the contribution of the stellar population is one of the first and most critical steps in the analysis of AGN emission-line spectra.

Here, we apply the same methods to subtract the stellar absorption lines by using a template derived from the galaxy itself. The template was scaled to the NLR spectra by normalisation in the red ($\sim$5400–5700 Å) justified by the fact that the slope at $\lambda \geq 5400$ Å does not change significantly for different stellar populations (Bica & Alloin 1986). Note that we also chose this range as it does not cover any strong NLR emission lines. To allow for a possible reddening difference of the template and each NLR spectrum due to different dust amounts in different galactic regions (or dust intrinsic to the NLR), we applied a reddening correction to the template by fitting the continuum slope of the template to the spectra of the NLR (MIDAS command "extinct/long" with extinction-law from Savage & Mathis 1979). Moreover, to take into account a mismatch in redshifts between the stellar template obtained from the outer portions of the galaxy and the underlying stellar absorption lines in the inner spectra, we corrected the redshift of the stellar template to the redshift of the inner spectra as measured by fitting a Gaussian to the absorption profile of Ca II K.
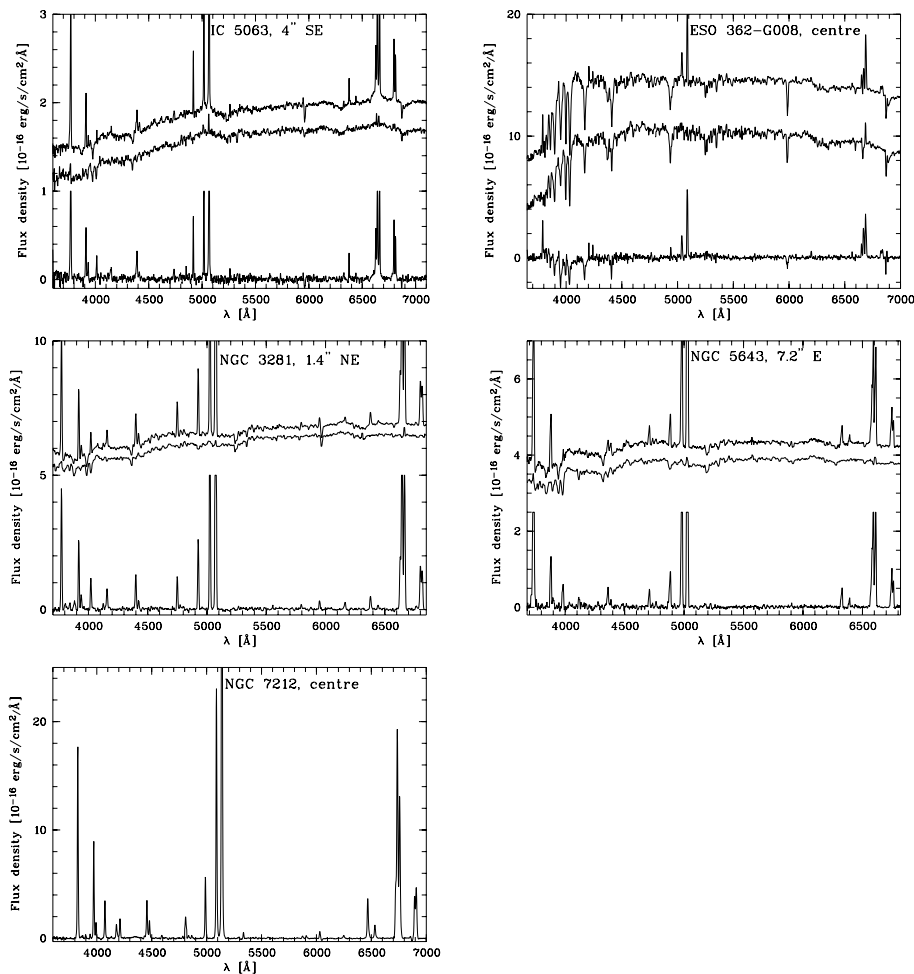
**Fig. 2.** Template subtraction for IC 5063, ESO 362-G008, NGC 3281, and NGC 5643. The observed (upper), the template (middle) and the template-subtracted spectra (lower spectrum) are shown. In these plots, both upper spectra are shifted vertically by an arbitrary amount. Strong emission lines are truncated in the difference spectrum. The template matches the stellar absorption lines seen in the NLR spectrum fairly well, with the exception of ESO 362-G008 for which strong Balmer absorption lines remain. For NGC 7212, no absorption features are distinguishable and thus no template was subtracted.

The procedure described above was generally applied (Table 3; Fig. 2) with the exception of NGC 7212 as no stellar absorption lines were seen in the spectra. For IC 5063, the Na I D absorption line was used to estimate the redshift difference between template and inner spectra as this is the only strong absorption line that can be followed throughout the region of interest. For NGC 5643, there is no absorption line within the spectral range that can be measured at a sufficient $S/N$. Therefore, the [O III] emission line was used to estimate the difference in velocities.

To probe the quality of the match between the stellar template and each observed NLR spectrum, we concentrated on stellar absorption lines which were not contaminated by emission throughout the NLR. Two strong lines suited for this purpose are Ca II K and Na I D. While the residuum of Ca II K absorption in the resulting spectrum after subtraction of the stellar template is within the noise levels, Na I D absorption remains in some objects (e.g. NGC 3281 and IC 5063). However, at least part of the Na I D absorption line may originate from interstellar absorption and can be strong in the regions of high reddening (Bica & Alloin 1986). Thus, we additionally checked that there are no remaining absorption features of the G band at 4300 Å and Mg I $\lambda$ 5176 Å. Indeed, any remaining putative absorption is within the noise limit, confirming our results from the Ca II K line.

The lack of significant other stellar absorption lines after subtraction of the template confirms that the stellar population does not change much throughout the NLR in the observed objects. One exception is ESO 362-G008: Here, the stellar population seems to change very rapidly in the innermost regions and the equivalent widths (EW) of the underlying Balmer absorption lines get significantly larger towards the centre. It implies the existence of a very young stellar population close to the AGN. It was not possible to derive a template spectrum neither from the outer part of the galaxy which fitted the stellar absorption lines throughout the NLR nor from the inner part due to the "contamination" by emission lines. Close to the centre, the Balmer emission lines start to fill the underlying absorption trough making it impossible to correct for the stellar absorption. We decided to use an outer template as first approach. Our results indicate that for H$\beta$ and H$\alpha$ the correction was not sufficient.

### 3.4. Emission-line fluxes and reddening

The fluxes of the pure emission-line spectra were measured as a function of distance from the nucleus by integrating along a Gaussian fit to the line profile. The fit routine "fit/spec" (Rousset 1992) was used for this purpose.

The uncertainties in deriving the fluxes were mostly caused by the placement of the continuum and were thus estimated as the product of the *FWHM* of the line and the root-mean square deviation of the local continuum fluxes. Gaussian error propagation was used to calculate the errors of subsequent parameters such as line ratios, ionisation parameter, etc. The resulting errors are in the range of ~1–15%. Note that we did not take into account uncertainties from stellar absorption correction and the quality of the Gaussian fits which was very good given the low spectral resolution of our data.

**Table 4.** Observed and reddening-corrected line intensity ratios relative to H$\beta^a$.

| Line | IC 5063 | | NGC 7212 | | ESO 362-G008 | | NGC 3281 | | NGC 5643 | | NGC 1386 | |
|------|---------|--------|----------|--------|--------------|--------|----------|--------|----------|--------|----------|--------|
| | $F_{\rm obs}$ | $F_{\rm dered}$ | $F_{\rm obs}$ | $F_{\rm dered}$ | $F_{\rm obs}$ | $F_{\rm dered}$ | $F_{\rm obs}$ | $F_{\rm dered}$ | $F_{\rm obs}$ | $F_{\rm dered}$ | $F_{\rm obs}$ | $F_{\rm dered}$ |
| [O II] $\lambda$3727 Å | 1.48 | 2.96 | 2.03 | 2.63 | 1.48 | 2.61 | 1.80 | 2.62 | $-^b$ | $-^b$ | 1.81 | 2.63 |
| [Ne III] $\lambda$3869 Å | 0.47 | 0.86 | 0.98 | 1.22 | $-^c$ | $-^c$ | 0.73 | 1.01 | $-^b$ | $-^b$ | 0.77 | 1.07 |
| [Ne III] $\lambda$3967 Å | 0.18 | 0.31 | 0.4 | 0.49 | $-^c$ | $-^c$ | 0.26 | 0.35 | $-^b$ | $-^b$ | 0.48 | 0.64 |
| [O III] $\lambda$4363 Å | 0.11 | 0.15 | 0.20 | 0.23 | $-^c$ | $-^c$ | 0.12 | 0.14 | $-^b$ | $-^b$ | 0.19 | 0.23 |
| He II $\lambda$4686 Å | 0.14 | 0.15 | 0.23 | 0.24 | $-^c$ | $-^c$ | 0.36 | 0.38 | $-^b$ | $-^b$ | 0.46 | 0.48 |
| [O III] $\lambda$5007 Å | 8.88 | 8.03 | 12.52 | 12.06 | 11.57 | 10.65 | 9.21 | 8.72 | 12.38 | 11.40 | 11.34 | 10.73 |
| [Fe VII] $\lambda$5721 Å | – | – | – | – | – | – | 0.08 | 0.06 | $-^b$ | $-^b$ | 0.29 | 0.22 |
| [Fe VII] $\lambda$6087 Å | 0.14 | 0.07 | 0.06 | 0.04 | – | – | 0.17 | 0.12 | $-^b$ | $-^b$ | 0.44 | 0.31 |
| [O I] $\lambda$6300 Å | 0.71 | 0.32 | 0.76 | 0.56 | 0.44 | 0.23 | 0.46 | 0.30 | $-^b$ | $-^b$ | 0.46 | 0.30 |
| [Fe X] $\lambda$6375 Å | 0.04 | 0.02 | 0.04 | 0.03 | – | – | 0.02 | 0.01 | $-^b$ | $-^b$ | 0.07 | 0.05 |
| H$\alpha$ | 7.10 | 2.87 | 4.04 | 2.87 | 6.06 | 2.87 | 4.71 | 2.87 | 6.03 | 2.87 | 4.70 | 2.87 |
| [N II] $\lambda$6583 Å | 4.27 | 1.71 | 2.82 | 1.99 | 6.78 | 3.18 | 4.02 | 2.44 | 6.30 | 2.98 | 5.60 | 3.41 |
| [S II] $\lambda$6716 Å | 1.51 | 0.58 | 0.80 | 0.56 | 1.19 | 0.54 | 1.31 | 0.78 | 1.74 | 0.80 | 1.04 | 0.62 |
| [S II] $\lambda$6731 Å | 1.49 | 0.57 | 0.98 | 0.63 | 1.53 | 0.70 | 1.24 | 0.74 | 1.94 | 0.89 | 1.29 | 0.77 |

$^a$ All narrow emission line ratios were derived from the nuclear spectra. After reddening correction, other Balmer line-ratios such as H$\gamma$/H$\beta$ and H$\delta$/H$\beta$ are consistent with the recombination values within the errors. The uncertainties are in the range of ~1–15%.
$^b$ Not covered by wavelength range.
$^c$ Underlying absorption lines.

**Table 5.** Reddening-corrected H$\beta$ luminosity and results from dereddened line ratios of the nuclear spectra.

| | IC 5063 | NGC 7212 | ESO 362-G008 | NGC 3281 | NGC 5643 | NGC 1386 |
|--|---------|----------|--------------|----------|----------|----------|
| $F_{\rm H\beta}$ ($10^{-14}$ erg s$^{-1}$ cm$^{-2}$) | $54 \pm 1$ | $12 \pm 0.5$ | $11.5 \pm 2$ | $36 \pm 1$ | $10 \pm 0.5$ | $99 \pm 7$ |
| $L_{\rm H\beta}$ ($10^{39}$ erg s$^{-1}$) | $140 \pm 3$ | $169 \pm 5$ | $65 \pm 9$ | $107 \pm 4$ | $4.8 \pm 0.3$ | $14.2 \pm 1$ |
| $T_{\rm e,obs}$ (K) | $13865 \pm 1800$ | $14635 \pm 1500$ | $-^a$ | $13715 \pm 440$ | $-^b$ | $15650 \pm 1500$ |
| $E_{B-V}$ (mag)$^c$ | $0.8 \pm 0.01$ | $0.3 \pm 0.01$ | $0.66 \pm 0.05$ | $0.44 \pm 0.01$ | $0.65 \pm 0.02$ | $0.43 \pm 0.02$ |
| $n_{\rm e,obs}$ (cm$^{-3}$) | $635 \pm 30$ | $1420 \pm 50^d$ | $1420\,(1710) \pm 70^e$ | $540 \pm 40$ | $860\,(1035) \pm 30^e$ | $1545 \pm 50$ |
| $U_{\log(n_e)=3,\rm obs}$ ($10^{-3}$) | $2.15 \pm 0.01$ | $3.27 \pm 0.02$ | $2.76 \pm 0.1$ | $2.3 \pm 0.02$ | $-^b$ | $2.83 \pm 0.01$ |

$^a$ Underlying absorption lines.
$^b$ Not covered by wavelength range.
$^c$ Note that this central value is not necessarily representative for the reddening within the NLR; for more details on reddening see Table 6.
$^d$ [S II] $\lambda$6716 Å is slightly truncated by telluric absorption bands.
$^e$ Using $T_e = 10\,000$ K and, in brackets, $\langle T_e \rangle_{\rm 4Sy2s} \sim 14\,465$, respectively.

The spectra were dereddened using the recombination value for the intensity ratio H$\alpha$/H$\beta$ = 2.87 (a typical value for $T_e$ = 10 000 K, Osterbrock (1989), Table 4.2) and an average reddening curve (Osterbrock (1989), Table 7.2). Note that in the following, only those spectra are used which have emission-line fluxes exceeding the *S/N* ratio of 3.

For NGC 5643 and IC 5063, a simple Gaussian was not sufficient to fit the observed narrow-line profiles. The profiles revealed substructure such as blue- or redshifted subpeaks and shoulders. This is a well known phenomenon for Seyfert galaxies (e.g. Whittle 1985; Veilleux 1990) and has recently also been found for quasars (Leipski & Bennert 2006). It is commonly interpreted as outflow and/or interaction with a radio jet. The pronounced substructure was limited to the central arcseconds (22″ for NGC 5643 and 9″ for IC 5063) and we used three Gaussians (a central one as well as a blueshifted and a redshifted one) to fit the narrow emission lines with the strengths varying spatially to closely approximate the total line flux. For NGC 5643, we were able to study the profiles and their spatial variation in greater detail, given the high resolution of these spectra (Appendix A.5).

## 4. Results and discussion

In the following, we include the results for the Seyfert 2 NGC 1386 from Paper I in the tables presented here for comparison. We do not show the corresponding figures for NGC 1386 but refer the reader to Paper I.

### 4.1. Nuclear spectra

Table 4 lists the observed and reddening-corrected line-intensity ratios relative to H$\beta$ from the nuclear spectrum (uncorrected for slit losses). For pairs of lines ([O III], [O I], and [N II]) with a fixed line ratio (~3:1), only the brighter line is shown. Emission-line ratios of the strongest lines as a function of distance from the centre can be found online for each individual galaxy (including NGC 1386).

In Table 5, we give the reddening-corrected H$\beta$ luminosity and summarise the results from dereddened line ratios such as the electron temperature $T_{\rm e,obs}$[6], the reddening value $E_{B-V}$, the electron density $n_{\rm e,obs}$, and the ionisation parameter $U_{\rm obs}$ for the

[6] Derived from the [O III]($\lambda$4959 Å+$\lambda$5007 Å)/$\lambda$4363 Å emission-line ratio.
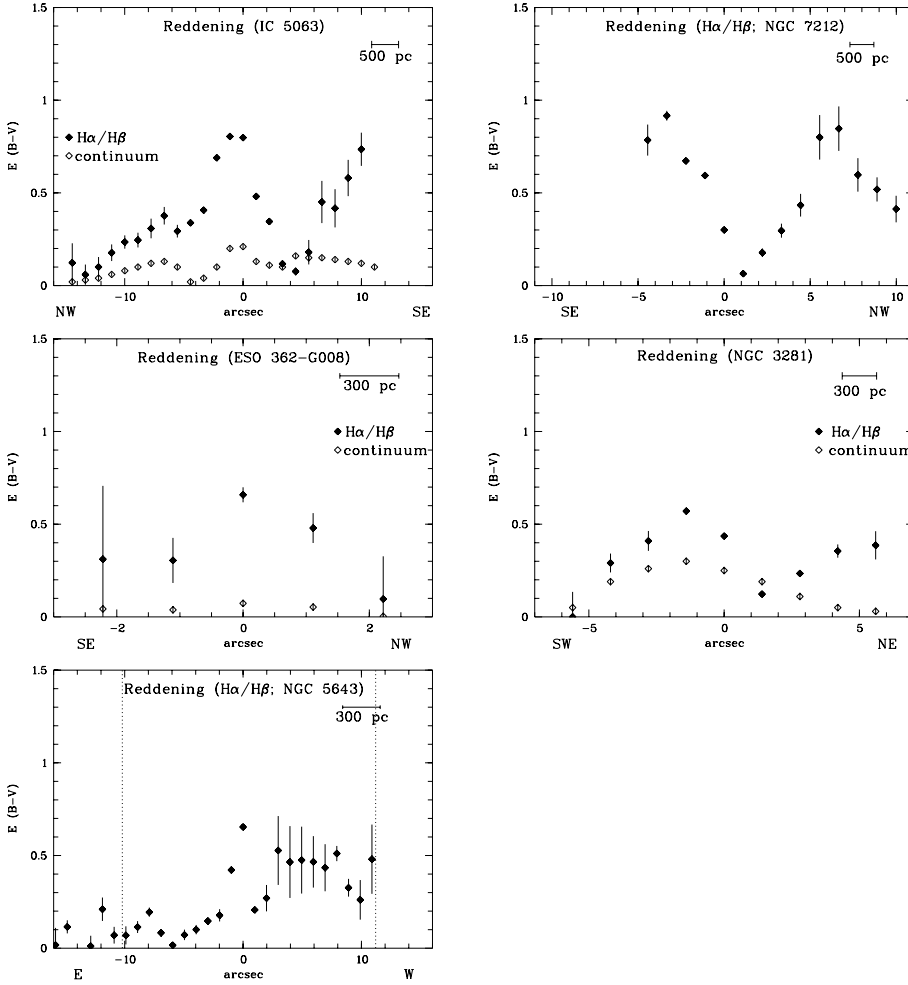
**Fig. 3.** Reddening distributions of the Seyfert-2 galaxies IC 5063, NGC 7212, ESO 362-G008, NGC 3281, and NGC 5643. The reddening was derived from the recombination value of the narrow Hα/Hβ emission-line ratio (filled symbols). For some objects, we are able to also show the reddening distribution of the continuum of the central spectra relative to the stellar template as determined during template subtraction (open symbols). For NGC 5643, the edge of the NLR as determined from the diagnostic diagrams is indicated by dotted lines.

nuclear spectra of all objects. The parameters represent an average over the central several hundred parsecs.

The temperature was, in most objects, only determined for the nuclear spectrum due to the faintness of the involved [O III] $\lambda4363$ Å emission line in the outer spectra. In some objects, we were able to derive the electron temperature in the inner few arcseconds (NGC 3281, NGC 7212, and IC 5063) where it stays roughly constant within the errors or scatters without showing a clear dependency on radius. The central temperature was used to apply a correction to the electron density. In those cases in which no temperature was measured we used $T_e = 10\,000\,\mathrm{K}$ or an average temperature derived from the other galaxies instead. The other values (reddening, electron density, and ionisation parameter) were determined throughout the NLR and we discuss each of them in turn.

### 4.2. Reddening distribution

Two different measures of reddening across the galaxy were derived: (i) the reddening of the continuum slope in the central parts with respect to the template derived in the outer parts of the galaxy; (ii) the reddening distribution obtained from the recombination value for the (narrow-line) intensity ratio Hα/Hβ. The first reddening value was only derived for those objects for which a stellar template correction was applied. The reddening distributions are shown in Fig. 3. While the nuclear reddening is given in Table 5, we give in Table 6 the highest reddening value within the NLR, the distance from the centre at which it occurs

**Table 6.** Maximum and global reddening within the NLR.

| Galaxy | max. $E_{B-V}$[a] (mag) | Distance[b] ($''$) | global $E_{B-V}$[c] (mag) |
|---|---|---|---|
| IC 5063 | 0.80 ± 0.01 | −1.11 | 0.39 ± 0.05 |
| NGC 7212 | 0.92 ± 0.03 | −3.33 | 0.56 ± 0.07 |
| ESO 362-G008 | 0.66 ± 0.04 | 0 | 0.39 ± 0.09 |
| NGC 3281 | 0.57 ± 0.02 | −1.4 | 0.33 ± 0.05 |
| NGC 5643 | 0.65 ± 0.01 | 0 | 0.30 ± 0.04 |
| NGC 1386 | 0.88 ± 0.2 | −4 | 0.48 ± 0.06 |

[a] Highest reddening value within the NLR.
[b] Distance from the centre at which highest reddening occurs.
[c] Derived by adding the Hα and Hβ flux within the NLR.

as well as the global reddening (as derived by summing the Hα and Hβ flux within the NLR).

As the match between the absorption lines of the stellar template and those seen in the spectra is quite close for all spectra, we believe that reddening by dust is the cause of the spatially varying continuum slope and not an intrinsically redder stellar population in the central part.

We cannot compare the absolute values of $E_{(B-V)}$ directly as the reddening determined from the continuum slope is a value relative to the template. The dispersion $\Delta E_{(B-V)}$ is significantly smaller than that obtained from the Balmer decrement. This can be due to extinction by foreground dust in e.g. the host galaxy which affects both the template and the central spectra and thus
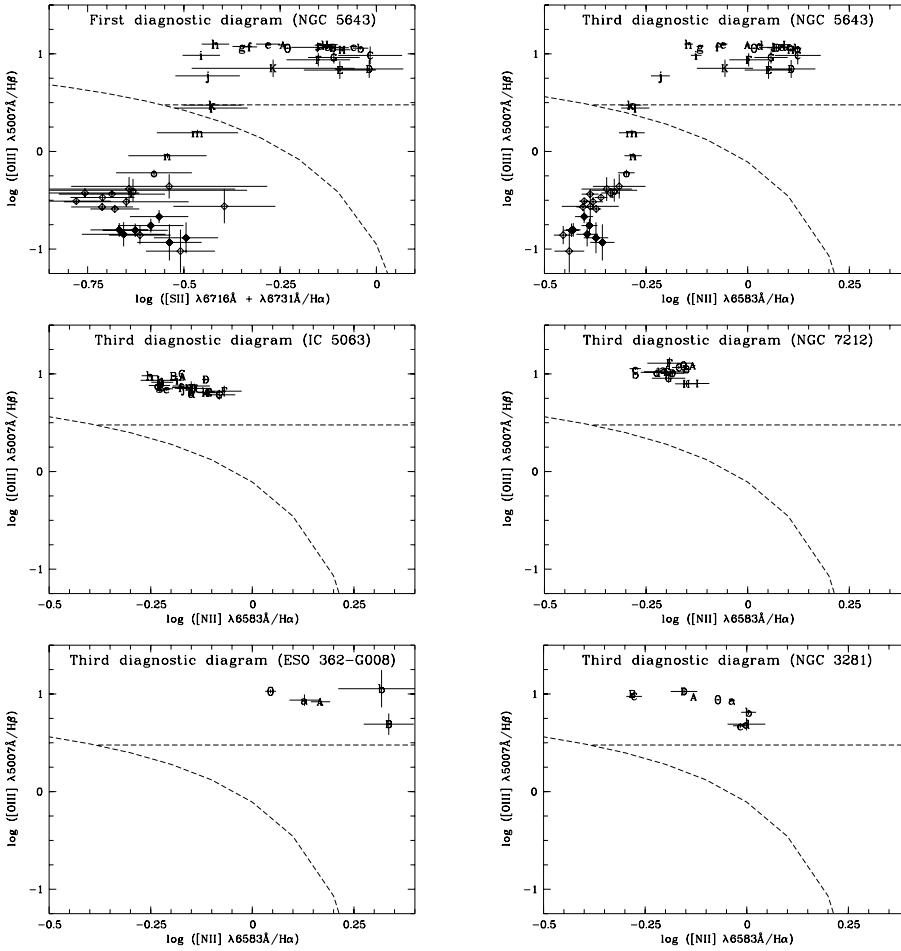
**Fig. 4.** Diagnostic diagrams for spatially-resolved emission-line ratios in NGC 5643 (first and third diagnostic diagram) as well as in IC 5063, NGC 7212, ESO 362-G008, and NGC 3281 (due to similarity, only third diagnostic diagram is shown).

do not reflect in the relative reddening value. However, often both reddening values are distributed differently indicating that the stellar population and the NLR are suffering different dust extinctions. As discussed in Paper I, the most probable explanation is dust intrinsic to the NLR clouds with a varying column density along the line-of-sight.

As in Paper I, we use the reddening distribution determined from the narrow Hα/Hβ emission-line ratio to correct for the intrinsic reddening of the NLR itself as these lines originate in the NLR and thus give a better estimate for the reddening within the NLR than the one determined from the continuum slope.

In some cases (e.g. NGC 5643, IC 5063), the reddening is highest in the centre and decreases with distance from the nucleus. But more often, the distributions show deviations from such a general trend.

For ESO 362-G008, the reddening correction $E_{(B-V)}$ needed to fit the continuum of the stellar template to that of the observed central spectra was set arbitrarily to zero in Fig. 3 for comparison. Note that in this object, the difference in slope between the continuum of the NLR and that of the stellar template may not entirely be due to dust but may at least partially be due to the change in stellar population: The continuum in the centre appears to be bluer than the template, reflecting the very young stellar population already mentioned earlier.

### 4.3. Spatially resolved spectral diagnostics

As in Paper I, we use diagnostic line-ratio diagrams of the three types pioneered by Baldwin et al. (1981) to not only distinguish between emission-line object classes (e.g. Seyfert galaxies,

LINERs, Starbursts, transition objects), but, to probe the "real" NLR size, i.e. the central region which is photoionised by the AGN, and to discriminate the contribution from starbursts.

The high $S/N$ ratio of our spectra enables us to measure line ratios for all three diagrams ("first": [O III]/Hβ versus [S II]/Hα; "second": [O III]/Hβ versus [O I]/Hα; "third": [O III]/Hβ versus [N II]/Hα) out to several arcseconds from the nucleus. We present typical diagnostic diagrams for all objects in Fig. 4. The symbols are chosen such that "O" refers to the central spectrum, the small letters mark regions corresponding to "-" arcseconds from the nucleus, the capital ones mark regions corresponding to "+" arcseconds from the nucleus (Table 7).

As for NGC 1386 (Paper I), we find a clear transition between line ratios falling in the AGN regime and those typical for H II regions for NGC 5643. The transition is not as sharp as for NGC 1386, but the line ratios are gradually changing from AGN-type to H II-like ratios with line ratios of two outer spectra falling in the corner between LINER, AGN and H II regions. For the other four galaxies, no such transition is observed but all emission-line ratios are typical for gas ionised by an AGN power-law continuum.

We use the diagnostic diagrams to determine the NLR size. The results are summarised in Table 7. For those objects which show a transition of emission-line ratios from the central AGN region to H II regions, this method gives a measure of the NLR size without [O III] contamination from circumnuclear starbursts: although H II regions may be present over the entire emission–line region, the AGN ionisation dominates in the innermost arcseconds, determining the size of the NLR.

**Table 7.** Results from diagnostic diagrams[a]

| Galaxy | "a/A" Distance (″) | "a/A" Orientation | $R_{\text{[OIII]}}$ Literature (″) | $R_{\text{[OIII]}}$ Our Data (″) | $R_{\text{line-ratios}}$ Our data (″) | $R_{\text{NLR}}$ Our Data (″, pc) |
|---|---|---|---|---|---|---|
| IC 5063 | 1 | NW/SE | 6[b] | 20 | 13 | >13 (2860) |
| NGC 7212 | 1 | SE/NW | 2.4[b] | 12 | 10 | >10 (5040) |
| ESO 362-G008 | 1 | SE/NW | 11.9[c] | 4 | 3 | >3 (960) |
| NGC 3281 | 1.4 | SW/NE | 3[b] | 9 | 5 | >5 (1180) |
| **NGC 5643** | 1 | E/W | 6[d] | 16 | 16 | **11 (1045)** |
| **NGC 1386** | 1 | S/N | 3[b] | 12 | 10 | **6 (310)** |

[a] The second column gives the distance from the centre to the first spectra (marked with the letters "a" and "A" in the diagnostic diagrams). In the third column, the orientation of the small and capital letters is listed. The maximum [O III] radius (*S/N* > 3) at the same PA taken from literature is given in the fourth column. We also give the [O III] radius (*S/N* > 3) observed from our spectra (Col. 5). In the sixth column, the radius is given until which we were able to plot line ratios in the diagnostic diagrams. In the last column, the radius of the NLR as determined from the diagnostic diagrams is given in ″ and, in brackets, pc, respectively. The two objects with a clear transition between NLR and H II region are marked in bold.

[b] Taken from HST image of Schmitt et al. (2003).

[c] Taken from groundbased image of Mulchaey et al. (1996).

[d] Taken from HST image of Simpson et al. (1997).

For both NGC 1386 and NGC 5643, which show a transition of line ratios, the determined NLR size is about twice as large as those measured from the HST snapshot survey of Schmitt et al. (2003), once again showing the low sensitivity of this survey. On the other hand, some authors have attributed all [O III] emission to the extended NLR. While for NGC 5643, Fraquelli et al. (2003) classify the [O III] line emission detected out to $r \sim 15$–$20''$ from longslit spectroscopy as extended NLR, we here show that [O III] emission beyond $r \sim 11''$ originates from H II regions. The same applies for NGC 1386: Fraquelli et al. (2003) determine the extended NLR from the observed [O III] line emission to $r \sim 10''$ while we can show that [O III] emission beyond $r \sim 6''$ is predominantly ionised by surrounding stars.

To conclude, compared to the spatially resolved spectral diagnostics measuring the "real" NLR size, the apparent NLR size determined by [O III] images can be either smaller in case of low sensitivity or larger in case of contributions of circumnuclear starbursts. A meaningful measure of the NLR size is of great importance to determine the slope, and thus the origin, of the NLR size-luminosity relation (Bennert et al. 2002). Moreover, it will help to probe whether indeed a different slope for type-1 and type-2 AGNs exist (Bennert et al. 2004, 2006b).

For the remaining four objects, the estimated NLR size is a lower limit. This points out the limits of the method presented here: The NLR radius determination depends on the relative brightness of the AGN and the central starburst component and therefore the NLR radius also depends on the presence, strength and distribution of starbursts. Such a method fails if there are no or just weak starforming regions surrounding the central AGN. In that case, we cannot say for sure whether the extension of the detected [O III] emission is limited by the competition between AGN and starburst luminosity.

### 4.4. Surface-brightness distribution

The spatially varying luminosities in the [O III] and Hα emission lines as well as the continuum (at 5450–5700 Å) were calculated and divided by the corresponding area in square parsecs at the galaxy to allow a comparison among all galaxies in our sample (Fig. 5). The surface-brightness distributions are similar to each other, centrally peaked and decreasing with distance from the nucleus.

For comparison, the [O III] surface-brightness distributions from the HST images of Schmitt et al. (2003) are shown for those objects included in the HST snapshot survey. They were derived by averaging three vectorplots along the major axis of the NLR emission. In all objects, they clearly show the higher spatial resolution of the HST image ($0\rlap{.}''05$–$0\rlap{.}''1$ pix$^{-1}$) compared to the 1–2″ spatial sampling of our spectral data. However, they also reveal the low sensitivity of the HST images compared to our spectroscopy: The [O III] emission at a *S/N* of 3 ends significantly earlier than what can be seen in our spectral data. In some cases, the HST [O III] surface-brightness distributions reveal several subpeaks of possibly individual NLR clouds, as can be already seen in the [O III] images (Fig. 1). These substructures are smoothed out in our ~10–20 times lower spatial resolution spectra but are nevertheless still visible as a secondary or tertiary peak, mostly in emission lines.

We fitted a power-law function $L = L_0(\frac{R}{R_0})^\delta$ (with projected radius $R$) to the surface-brightness distributions of [O III], Hα, and the continuum. The fitting parameters are shown in Table 8 (with $L_0$ referring to $R_0 = 100$ pc from the nucleus). Only data points within the NLR were included and taken as average from both sides of the nucleus. The [O III] surface brightness falls faster with radius than the Hα surface brightness and also faster than the continuum ($\langle\delta_{\text{[OIII]}}\rangle \sim -2.24 \pm 0.2$; $\langle\delta_{\text{Hα}}\rangle \sim -2.16 \pm 0.2$; $\langle\delta_{\text{cont}}\rangle \sim -1.19 \pm 0.1$).

This general trend is comparable to what has been found by Fraquelli et al. (2003) in their long-slit spectroscopic study of the NLR of 18 Seyfert-2 galaxies. However, they find on average a slightly steeper slope for especially [O III] ($\langle\delta_{\text{[OIII]}}\rangle \sim -3.6$; $\langle\delta_{\text{Hα}}\rangle \sim -2.6$; $\langle\delta_{\text{cont}}\rangle \sim -1.4$; calculated from their Table 2). This discrepancy can have different reasons. For one, we extracted spectra at every ~1″, whereas they extracted spectra at every ~2″. Secondly, the samples differ and only two objects are common to both samples. Thirdly, Fraquelli et al. (2003) include all visible emission in their fit, not concentrating on the NLR alone as they do not have a quantitative measure of the NLR size. Therefore, they possibly include [O III] emission from surrounding H II regions where the surface brightness drops significantly. This explanation is supported when comparing the results for NGC 1386 and NGC 5643, common to both samples: Fraquelli et al. (2003) report a steeper slope in the [O III] surface-brightness distribution but include emission out to
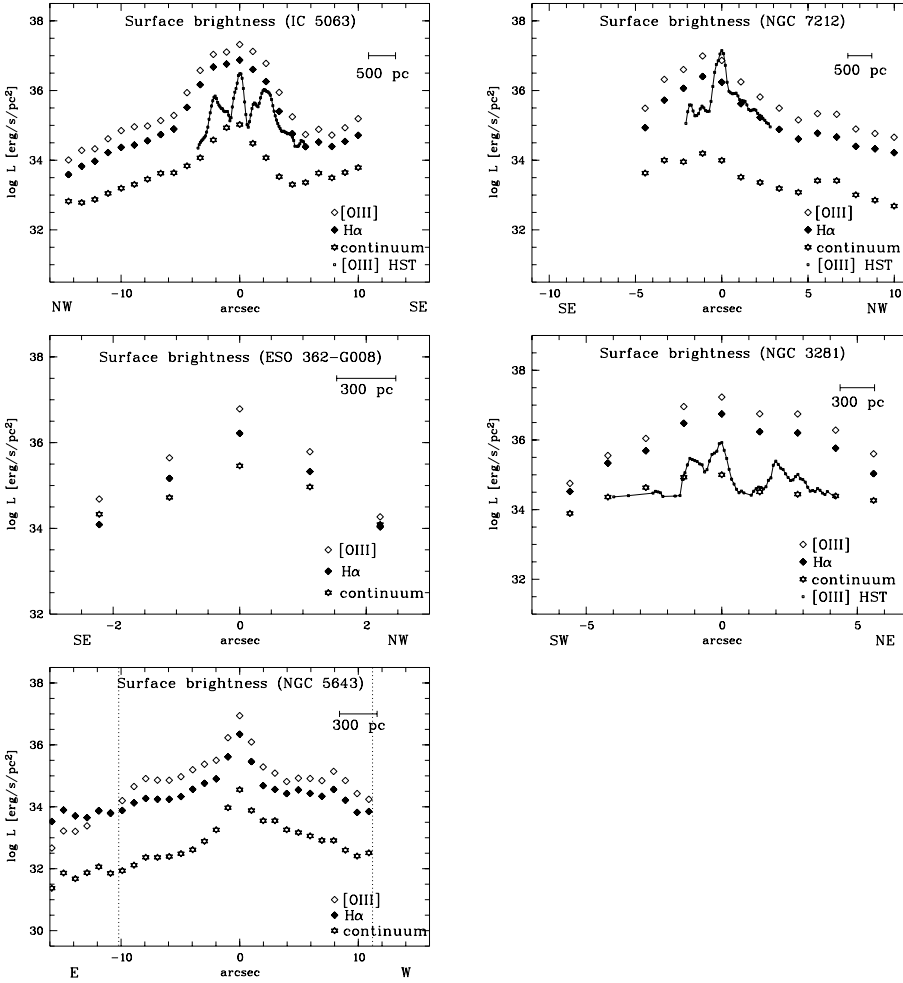
**Fig. 5.** Surface-brightness distributions of IC 5063, NGC 7212, ESO 362-G008, NGC 3281, and NGC 5643 in [O III] (open diamonds), Hα (filled diamonds), and continuum (at 5450–5700 Å, stars). The [O III] surface-brightness distribution from the HST image is shown as small open squares connected by a line (HST pixel scale ~ 0″.1 pix$^{-1}$). Only data points with $S/N > 3$ were included. Error bars are smaller than the symbol size. The HST image has a 10 to 20 times higher spatial resolution but a significantly lower sensitivity, not allowing to measure the outer parts of the NLR. Note that ESO 362-G0008 and NGC 5643 are not included in the HST snap-shot survey by Schmitt et al. (2003). For NGC 5643, the edge of the NLR as determined from the diagnostic diagrams is indicated by dotted lines.

**Table 8.** Fitting parameters of surface-brightness distributions[a]. For ESO 362-G008, too few data points were available for a fit.

| Galaxy | Data Points | $\delta_{\text{[OIII]}}$ | $\log L_{\text{[OIII]},0}$ (erg s$^{-1}$ pc$^{-2}$) | $\delta_{\text{H}\alpha}$ | $\log L_{\text{H}\alpha,0}$ (erg s$^{-2}$ pc$^{-2}$) | $\delta_{\text{cont}}$ | $\log L_{\text{cont},0}$ (erg s$^{-2}$ pc$^{-2}$) |
|---|---|---|---|---|---|---|---|
| IC 5063 | 9 | $-2.73 \pm 0.33$ | 38.41 | $-2.75 \pm 0.31$ | 38.01 | $-1.37 \pm 0.18$ | 35.2 |
| NGC 7212 | 4 | $-2.13 \pm 0.57$ | 38.46 | $-2.09 \pm 0.56$ | 37.85 | $-0.77 \pm 0.26$ | 34.57 |
| NGC 3281 | 4 | $-2.35 \pm 0.60$ | 38.22 | $-2.34 \pm 0.64$ | 37.73 | $-1.02 \pm 0.18$ | 35.34 |
| NGC 5643 | 10 | $-1.42 \pm 0.19$ | 35.97 | $-1.34 \pm 0.16$ | 35.35 | $-1.54 \pm 0.11$ | 33.94 |
| NGC 1386 | 6 | $-2.56 \pm 0.82$ | 37.16 | $-2.27 \pm 0.60$ | 36.55 | $-1.26 \pm 0.48$ | 35.46 |

[a] A linear least-squares fit was applied with $\log L = \delta \cdot \log R/R_0 + \log L_0$ and $R_0 = 100$ pc from the nucleus. The number of data points included in the fit is given in Col. 2 (=half the number of averaged values from both sides of the nucleus). For NGC 5643 which shows a transition between line ratios typical for AGNs and H II-regions, only data points within the NLR were included.

distances from the nucleus where we can show from diagnostic diagrams that this emission can be attributed to surrounding H II regions.

### 4.5. Electron-density distribution

Applying the classical methods outlined in Osterbrock (1989), we derive the electron density as a function of distance to the nucleus using the ratio of the [S II] $\lambda\lambda6716,6731$ Å pair of emission lines. We used the observed central temperature to correct for the dependency of electron density on temperature[7]. Due to the faintness of the involved [O III] $\lambda4363$ Å emission line, we were not able to measure the temperature in the outer parts. For

[7] $n_e(T) = n_e(\text{[SII] ratio}) \cdot \sqrt{(T/10\,000)}$.

those objects for which no temperature was determined, we assumed $T_e = 10\,000$ K.

In all objects, the electron density is highest at the nucleus and decreases outwards down to the low-density limit (assumed to be 50 cm$^{-3}$; Fig. 6). In some cases, it reveals a secondary or tertiary peak on one or both sides of the optical centre. A characteristic structure with a central peak and two smaller peaks on both sides of the nucleus can be identified in three objects (IC 5063, NGC 5643, and NGC 1386 (Paper I)). The outer peaks are often close to the boundary of the NLR. These density enhancements may indicate shocks occurring at the edge of the NLR.

In Table 9, we give the results of fitting a power-law function $n_{e,\text{obs}} = n_{e,0}(\frac{R}{R_0})^\delta$ to the observed electron densities (with $n_{e,0}$ at $R_0 = 100$ pc from the nucleus). We included only data points
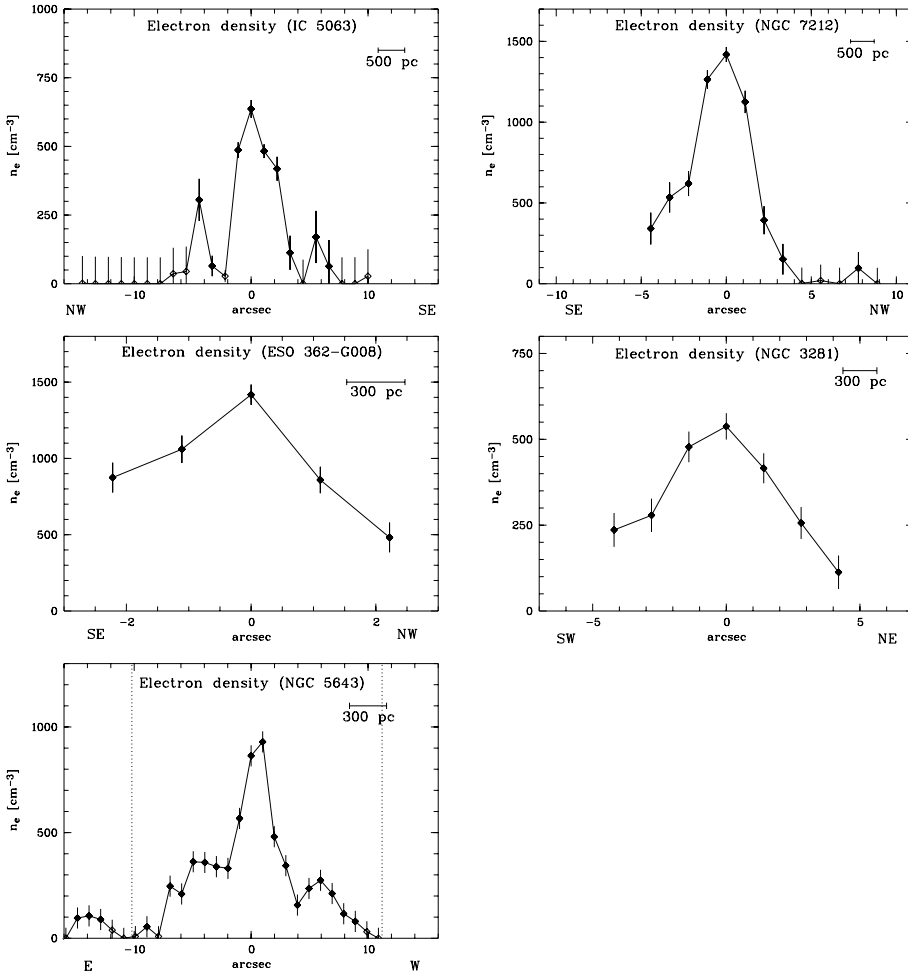
**Fig. 6.** Electron density obtained from the [S II] $\lambda6716\,\text{Å}/\lambda6731\,\text{Å}$ ratio as a function of the distance from the nucleus for IC 5063, NGC 7212, ESO 362-G008, NGC 3281, and NGC 5643. Open symbols indicate locations where $n_{e,obs}$ is in the low-density limit (assumed $\leq 50\,\text{cm}^{-3}$). For NGC 5643, the edge of the NLR as determined from the diagnostic diagrams is indicated by dotted lines.

within the NLR and averaged the electron densities from both sides of the nucleus. $\delta$ ranges between $-0.8$ and $-1.3$. On average, the density decreases with $R^{-1.14\pm0.1}$. These results are comparable to those of Fraquelli et al. (2003) who give power-law fits to electron densities of 14 Seyfert-2 galaxies.

The temperature can be a function of distance from the central AGN. Unfortunately, we are not able to determine the temperature dependency on distance from the nucleus. In those objects where we are able to trace the electron temperature in the inner few arcseconds, it remains roughly constant. One may expect that the temperature is decreasing if the AGN is the only heating source. In that case, correcting with the central temperature overestimates the electron density in the outer parts. The observed decreasing slope can therefore not be artificially introduced by a wrong temperature correction. On the other hand, some authors report an increasing temperature with distance from the nucleus (e.g. Bergeron et al. 1983) and explain it with a decrease in electron density faster than $n_e \propto r^{-2}$. However, the average decrease of electron density $n_{e,obs}$ we observe is with $\delta \sim -1.1$ slower than that.

Note that the critical density for [S II] $\lambda\lambda6716,6731\,\text{Å}$ is $\sim 1500\,\text{cm}^{-3}$ and $3900\,\text{cm}^{-3}$, respectively. Thus, these lines can only be used to measure the density in an environment with densities below $\sim 1500\,\text{cm}^{-3}$. For some objects in which we measure central densities in this regime, the central density may thus be underestimated.

**Table 9.** Fitting parameters of electron-density distribution[a]

| Galaxy | Data points | $\delta$ | $\log n_{e,0}$ (cm$^{-3}$) |
|--------|-------------|----------|----------------------------|
| IC 5063 | 6 | $-1.08 \pm 0.25$ | 3.1 |
| NGC 7212 | 4 | $-1.33 \pm 0.15$ | 4.1 |
| NGC 3281 | 3 | $-0.84 \pm 0.08$ | 3.1 |
| NGC 5643 | 10 | $-1.22 \pm 0.30$ | 3.0 |
| NGC 1386 | 5 | $-1.23 \pm 0.09$ | 2.4 |

[a] A linear least-squares fit was applied with $\log n_{e,obs} = \delta \cdot \log R/R_0 + \log n_{e,0obs}$. $n_{e,0}$ corresponds to the value at $R_0 = 100$ pc distance from the centre. The number of data points included in the fit is given in Col. 2 (=half the number of averaged values from both sides of the nucleus). For those objects which show a transition between line ratios typical for AGNs and H II-region like ones in the diagnostic diagrams, determining the size of the NLR, only data points within the NLR were included (NGC 5643 and NGC 1386).

### 4.6. Ionisation-parameter distribution

The line ratio [O II]$\lambda3727\,\text{Å}$/[O III] $\lambda5007\,\text{Å}$ can be used to estimate the value of the ionisation parameter $U$ (e.g. Penston et al. 1990; Komossa & Schulz 1997). Here, we follow the method described in Paper I.

In most objects, the ionisation parameter peaks at the optical nucleus and decreases with distance. The two exceptions are the Seyfert-2 galaxies NGC 3281 and IC 5063 where the ionisation parameter reaches its maximum value several arcseconds to one side of the centre. However, the optical nucleus needs not
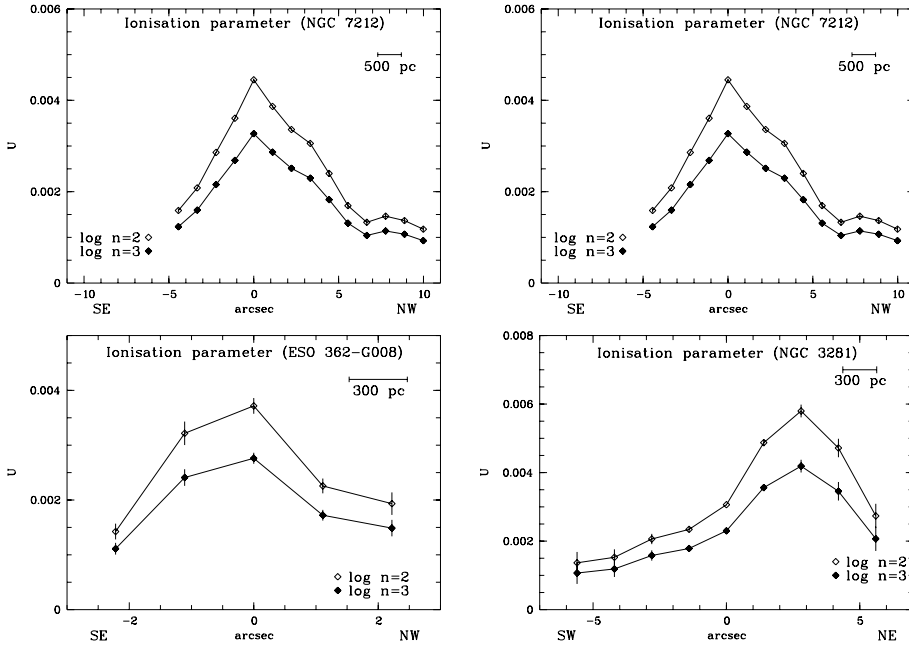
**Fig. 7.** Ionisation parameter derived from [O II]/[O III] ratio as a function of the distance from the nucleus for IC 5063, NGC 7212, ESO 362-G008, and NGC 3281 (open symbols: $n_H = 100\,cm^{-3}$, filled ones: $n_H = 1000\,cm^{-3}$). The edge of the NLR as determined from the diagnostic diagrams is indicated by dotted lines. Note that for NGC 5643, the [O II] line was not included in the observed spectral range and we cannot present the ionisation parameter.

**Table 10.** Fitting parameters of ionisation-parameter distribution[a].

| Galaxy | Data points | $\delta$ | $\log U_0$ |
|---|---|---|---|
| NGC 7212 | 4 | $-0.43 \pm 0.08$ | $-2.1$ |
| NGC 1386 | 6 | $-0.58 \pm 0.03$ | $-2.7$ |

[a] A linear least-squares fit was applied with $\log U_{\log(n_e)=2,\mathrm{obs}} = \delta \cdot \log R/R_0 + \log U_0$. $U_0$ corresponds to the value at $R_0 = 100$ pc distance from the centre. The number of data points included in the fit is given in column 2 (= half the number of averaged values from both sides of the nucleus). For NGC 1386 which shows a transition between line ratios typical for AGNs and H II-regions, only data points within the NLR were included. For ESO 362-G008, too few data points were available for a fit. For NGC 3281 and IC 5063, no fit was applied as the ionisation parameter does not peak in the centre. For NGC 5643, the [O II] line was not covered by the observations.

necessarily coincide with the position of the ionising source, the AGN, which may also be hidden by dust. We will discuss this issue when discussing the objects individually.

We fitted a power-law function $U_{\log(n_e)=2,\mathrm{obs}} = U_0(\frac{R}{R_0})^\delta$ to the observed ionisation parameter (with $R_0 = 100$ pc from the nucleus; Table 10). We include only data points within the NLR and averaged the ionisation parameters of both sides of the nucleus. $\delta$ ranges between $-0.4$ and $-0.6$. Note that we did not measure the slope of the ionisation parameter in the Seyfert-2 galaxies NGC 3281 and IC 5063 as the ionisation parameter does not peak in the centre. We could not determine the ionisation parameter for NGC 5643 as the [O II] $\lambda3727$Å emission line is not covered by the spectral range.

### 4.7. Velocities

We derived the NLR line-of-sight velocity curve by taking the average of velocity centroids derived by fitting Gaussians to Hα and [N II] emission lines. For comparison, we also show the velocity curve derived in the same manner from the [O III] emission line which may hint at NLR-jet interaction. In addition, given the high S/N ratio of our spectra, we were able to trace the stellar rotation curves from Gaussian fits to the stellar absorption lines

Ca II K or Na I D for three objects (before subtraction of the stellar template) throughout the whole region as these lines are not blended with emission lines. The results are shown in Fig. 8. We estimated the uncertainty in determining the velocity peaks to $\sim 20\,\mathrm{km\,s^{-1}}$ for both the emission and absorption lines. Note that for ESO 362-G008, the Hα line suffers from the underlying absorption line which was not well subtracted in all regions and thus, only [N II] was used. The velocity determined from the [O III] line is limited to the central $4''$ due to low S/N in the outer parts.

Detailed interpretation of the NLR velocity curves is beyond the scope of this paper. Even for very simple gas distributions, like a disk with circular rotation, NLR line-of-sight velocity fields can be quite complex due to collimation of the radiation field, dust obscuration and projection effects whose understanding requires modelling the 3D structure of the NLR with many degrees of freedom (position angle and inclination of the gaseous disk, opening angle, inclination and position angle and length of the ionisation cone, radial density profile, dust distribution, just to mention the most important ones). Moreover, outflows, random motions or elliptical streaming due to barred potentials might complicate the picture.

We will present such a modelling in a subsequent paper. Here, we limit ourselves to point out that all the galaxies show large-scale velocity gradients across their NLR. Based on our preliminary modelling, we believe that to the zeroth order, all of them can be explained by rotation (though we cannot rule out outflow components in some cases). The rotation interpretation is supported by the fact that in two objects for which we measure the stellar rotation curve (IC 5063, ESO 362-G008), this curve has similar behaviour as that for the gas: although the stellar velocity gradient is shallower, the NLR gas shows a component rotating in the same sense as the stars. The shallower slope of the stellar rotation curve can result from a different line-of-sight path through stellar and gaseous disks. Also the bulge stars modify the stellar rotation curve: all our galaxies have large bulges and if both bulge and disk stars are present along a given line-of-sight, the velocity centroid of the resulting absorption lines will be shifted towards lower values compared to disk stars alone.
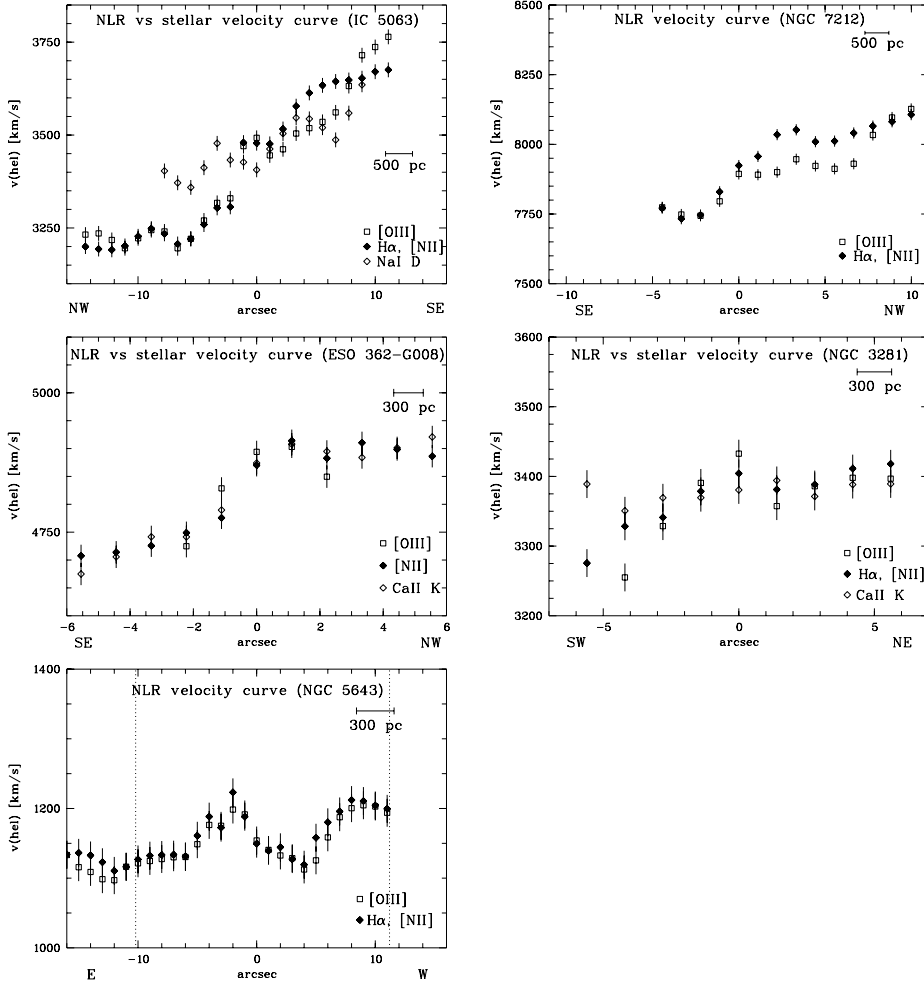
**Fig. 8.** Velocity fields of the Seyfert-2 galaxies IC 5063, NGC 7212, ESO 362-G008, NGC 3281, and NGC 5643. The velocities of the NLR were derived from the average value of the peak wavelengths of the Hα and [N II] emission lines (filled diamonds), with the exception of ESO 362-G008 where only [N II] was used. The [OIII] velocities are also shown (open squares). The stellar velocities were in most cases determined from the Ca II K absorption line "peak wavelength" as seen in the "raw" spectrum (open diamonds) if visible at a good S/N with the exception of IC 5063 where Na I D was used instead. For NGC 5643, the edge of the NLR as determined from the diagnostic diagrams is indicated by dotted lines.

## 5. Conclusions

We study high-sensitivity spatially-resolved spectra along the extended [O III] emission of six Seyfert-2 galaxies obtained with the VLT and the NTT. To derive the pure emission-line fluxes, we successfully use the galaxy itself as stellar template to subtract the underlying absorption lines in four out of six objects.

The nuclear spectra reveal the typical strong NLR emission from oxygen at different ionisation states, lines from ionised nitrogen and sulphur, as well as Balmer lines. In most objects, high-excitation iron lines are additionally seen in the central spectra, originating from the powerful and hard ionisation source in the centre.

Plotting line-ratios from our spatially resolved spectra in diagnostic diagrams, we observe a transition of emission-line ratios from the central AGN region to H II region in another Seyfert-2 galaxy (NGC 5643), in addition to the Seyfert-2 galaxy NGC 1386 already discussed in Paper I. The most probable explanation for this transition is that the stellar ionisation field starts to dominate that of the AGN. We are thus able to determine the radius of the NLR independent of sensitivity and excluding [O III] contamination from circumnuclear starbursts. In former spectroscopic studies, the observed [O III] has often been attributed to the extended NLR. We can show that at least part of this "extended NLR" emission is actually powered by H II regions and that only the central few arcseconds are indeed gas photoionised by the AGN.

In the other four objects, no such transition is observed but the line ratios fall in the AGN regime in all three diagnostic diagrams. Thus, the determined NLR size (1000-5000 pc) is a lower limit, limited by either the S/N of our data or the lack of a strong surrounding stellar ionisation field.

We derive physical parameters of the NLR such as reddening, surface brightness, electron density, and ionisation parameter as a function of projected distance from the nucleus. The differences between the reddening distributions determined from the continuum slope and the Balmer decrement argue in favour of dust intrinsic to the NLR with a varying column density along the line-of-sight. In most cases, both electron density and ionisation parameter decrease with radius.

In all the objects, the gas rotation curve shows a large-scale velocity gradient suggestive of rotation (though the detailed modelling was not carried out and some outflow might be present too). This is an important hint that the NLR gas is distributed in a disk rather than a sphere, an issue that is still a matter of debate.

We discuss the results for each object (see Appendix). In individual objects, substructures are seen in both the ionisation parameter and electron density and can often be interpreted as signs of shocks from the interaction of a radio jet and the NLR gas.

Our results for the five Seyfert-2 galaxies show that the NLR properties of the Seyfert-2 galaxy NGC 1386 in Paper I can be considered as prototypical, putting our conclusions on a larger statistical basis. We performed a similar study of the NLR of six Seyfert-1 galaxies. The comparison with the results presented

here will be summarised in Bennert et al. (2006c). All results presented here are described and discussed in detail in Bennert (2005).

# References

Antonucci, R. R. J. 1983, Nature, 303, 158
Antonucci, R. R. J. 1993, ARA&A, 31, 473
Baldwin, J. A., Phillips, M. M., & Terlevich, R. 1981, PASP, 93, 5
Ballantyne, D. R., Weingartner, J. C., & Murray, N. 2003, A&A, 409, 503
Bennert, N. 2005, Ph.D. Thesis, University of Bochum, Germany
Bennert, N., Falcke, H., Schulz, H., Wilson, A. S., & Wills, B. J. 2002, ApJ, 574, L105
Bennert, N., Falcke, H., Shchekinov, Y., & Wilson, A.S. 2004, IAUS, 222, 307B
Bennert, N., Jungwiert, B., Komossa, S., Haas, M., & Chini, R. 2006a, A&A, 446, 919 (Paper I)
Bennert, N., Jungwiert, B., Komossa, S., Haas, M., & Chini, R. 2006b, New Astron. Rev., in press
Bennert, N., Jungwiert, B., Komossa, S., Haas, M., & Chini, R. 2006c, A&A, submitted
Bergeron, J., Durret, F., & Boksenberg, A. 1983, A&A, 127, 322
Bica, E. 1988, A&A, 195, 76
Bica, E., & Alloin, D. 1986, A&A, 166, 83
Bowen, I. S. 1960, ApJ, 132, 1
Cid Fernandes, R., Storchi-Bergmann, T., & Schmitt, H. R. 1998, MNRAS, 297, 579
Cid Fernandes, R., Heckman, T. M., Schmitt, H. R., González Delgado, R. M., & Storchi-Bergmann, T. 2001, ApJ, 558, 81
Colbert, E. J. M., Baum, S. A., Gallimore, J. F., et al. 1996, ApJS, 105, 75
Colina, L., Sparks, W. B., & Macchetto, F. 1991, ApJ, 370, 102
De Vaucouleurs, G., De Vaucouleurs, A., Corwin, H. G., et al. 1991, Third Reference Catalogue of Bright Galaxies, Vol. III (New York: Springer Verlag) (RC3)
Durret, F., & Bergeron, J. 1988, A&AS, 75, 273

Durret, F., & Warin, F. 1990, A&A, 238, 15
Falcke, H., Wilson, A. S., & Simpson, C. 1998, ApJ, 502, 199
Ferland G. J., Korista K. T., Verner D. A., et al. 1998, PASP, 110, 761
Filippenko, A. V. 1982, PASP, 94, 715
Fraquelli, H. A., Storchi-Bergmann, T., & Binnette, L. 2000, ApJ, 532, 867
Fraquelli, H. A., Storchi-Bergmann, T., & Levenson, N. A. 2003, MNRAS, 341, 449
Inglis, M., Hough, J. H., Axon, D. J., Bailey, J., & Ward, M. J. 1993, MNRAS, 263, 895
Keel, W. C. 1996, AJ, 111, 2
Komossa, S., & Schulz, H. 1997, A&A, 323, 31
Kulkarni, V. P., Calzetti, D., Bergeron, L., et al. 1998, ApJ, 492, L121
Leipski, C., & Bennert, N. 2006, A&A, 448, 165
Leipski, C., Falcke, H., Bennert, N., & Hüttemeister, S. 2006, A&A, 455, 161
Malkan, M. A., Gorjian, V., & Tam, R. 1998, ApJS, 117, 2588
Morganti, R., Osterloo, T., & Tsvetanov, Z. I. 1998, AJ, 115, 915
Morris, S., Ward, M., Whittle, M., Wilson, A. S., & Taylor, K. 1985, MNRAS, 216, 193
Mulchaey, J. S., Wilson, A. S., & Tsvetanov, Z. I. 1996, ApJS, 102, 309
Nagar, N. M., Wilson, A. S., Mulchaey, J. S., & Gallimore, J. F. 1999, ApJS, 120, 209
Osterbrock, D. E. O. 1989, Astrophysics of Gaseous Nebulae and Active Galactic Nuclei (Mill Valley: University Science Books)
Penston, M. V., Robinson, A., Alloin, D., et al. 1990, A&A, 236, 53
Quillen, A. C., Alonso-Herrero, A., Rieke, M. J., et al. 1999, ApJ, 525, 685
Rousset, A. 1992, Ph.D. Thesis, Univ. J. Monnet de Saint-Étienne
Savage, B. D., & Mathis, J. S. 1979, ARA&A, 17, 73
Schlegel, D. J., Finkbeiner, D. P., & Davis, M. 1998, ApJ, 500, 525
Schmitt, H. R. 1998, ApJ, 506, 647
Schmitt, H. R., Storchi-Bergmann, T., & Baldwin, J. A. 1994, ApJ, 423, 237
Schmitt, H. R., Ulvestad, J. S., Antonucci, R. R. J., & Kinney, A. L. 2001, ApJS, 132, 199
Schmitt, H. R., Donley, J. L., Antonucci, R. R. J., Hutchings, J. B., & Kinney, A. L. 2003, ApJS, 148, 327
Simpson, C., Wilson, A. S., Bower, G., et al. 1997, ApJ, 474, 121
Storchi-Bergmann, T., Wilson, A. S., & Baldwin, J. A. 1992, ApJ, 396, 45
Storchi-Bergmann, T., Raimann, D., Bica, E. L. D., & Fraquelli, H. A. 2000, ApJ, 544, 747
Tran, H. D. 1995, ApJ, 440, 578
Tran, H. D., Miller, J. S., & Kay, L. E. 1992, ApJ, 397, 452
Tsvetanov, Z. I., & Petrosian, A. R. 1995, ApJS, 101, 287
Tüg, H. 1997, ESO Messenger No. 11, p.7
Ulvestad, J. S., & Wilson, A. S. 1984, ApJ, 278, 544
Veilleux, S. 1990, PASP, 102, 494
Viegas-Aldrovandi, S. M., & Contini, M. D. 1989, A&A, 215, 253
Vignali, C., & Comastri, A. 2002, A&A, 381, 834
Wagner, S. J., & Appenzeller, I. 1989, A&A, 225, L13
Wasilewski, A. J. 1981, PASP, 93, 560
Whittle, M. 1982, Ph.D. Thesis, Cambridge University
Whittle, M. 1985, MNRAS, 213, 1

# Online Material

# Appendix A: Comments on individual objects

We searched the available literature for all objects in our sample and here summarise the most important results in comparison with our study (excluding NGC 1386 which was discussed in Paper I). Note that the velocity fields will be discussed in detail when comparing them to those derived from modelling in a subsequent paper.

## A.1. IC 5063

IC 5063 is a Seyfert-2 galaxy with a hidden BLR seen in polarised light (Inglis et al. 1993). Its radio luminosity is two orders of magnitude greater (Colina et al. 1991) than that typical of nearby Seyferts (Ulvestad & Wilson 1984). Thus, IC 5063 is also classified as narrow-line radio galaxy (NLRG).

Bergeron et al. (1983) studied the extended ionised gas with long-slit spectroscopy. Ionised gas is reported out to a distance of 19 kpc to the north-west of the nucleus (~60″ using their adopted distance to the galaxy and Hubble constant) and 9 kpc (~36″) to the south-east. Bergeron et al. (1983) find both an increasing temperature and ionisation parameter with increasing distance from the nucleus. Under the assumption of one central ionising source, this implies that the gas density decreases faster than $n_e \propto r^{-2}$.

Wagner & Appenzeller (1989) report the detection of an off-nuclear broad emission-line region at 1″.8 north-west of the nucleus. They interpret this emission as an extreme example of scattered nuclear emission with a very high intrinsic line emission from the nucleus. The enhanced nuclear activity, the irregular gas motions, and strong obscuration and scattering effects are interpreted as IC 5063 being a recent merger remnant.

Colina et al. (1991) used high spatial resolution optical and infrared imaging as well as optical spectroscopy to study the physical and kinematic conditions of the ionised gas. They find a highly anisotropic ionising radiation field with a conical morphology and an opening angle of 50° along a PA of 120°. The cone axis coincides with the photometric major axis of the galaxy (PA = 116°; RC3). The ionised gas extends over $d \simeq 69″$. Inside the cone, the excitation conditions are roughly uniform but drop very rapidly outside. The results of Colina et al. (1991) are similar to that of Bergeron et al. (1983), confirming a positive excitation gradient outwards from the nucleus. However, the observed radial dependency of the electron density along PA = 109° suggest $n_{e,obs} \propto R^{\delta}$ with $\delta = -0.6$. This is not consistent with the requirement of $\delta < -2$, needed to explain the increasing ionisation parameter. They suggest that a combined effect of decreasing density and abundance may explain the increasing excitation outwards from the nucleus. Several dust lanes are concentrated in the northern side of IC 5063, running approximately parallel to the major optical axis. High-excitation [Fe VII] and [Ca V] emission lines are detected in the central arcseconds.

The 3.6 cm radio map reveals a linear triple radio structure extending over 4″, associated with the NLR (Morganti et al. 1998). At 21 cm, broad blueshifted H I absorption is visible, indicating a fast net outflow. In the central region, there is clear evidence for a strong interaction between the radio jet and the ISM. The shock scenario is supported by HST/NICMOS observations by Kulkarni et al. (1998) who find three emission-line regions in [Fe II], Paα, and $H_2$ along the major axis aligned with knots seen in radio emission. The NICMOS data show a very red point source in the nucleus of IC 5063, interpreted as dust-obscured active nucleus.

A groundbased [O III] image was presented by Morganti et al. (1998), confirming the result of Colina et al. (1991) that the high-ionisation line-emitting gas has an "X-shaped" morphology with a basic symmetry axis of PA ~ 120°. The ionised gas can be traced out to a distance larger than $r \sim 30″$. Although the HST [O III] image from Schmitt et al. (2003) reveals the same shape, the [O III] extension is the fifth part of the groundbased one ($r \sim 6″$). Schmitt et al. (2003) explain the small size by the limited field-of-view of the linear-ramp filter (~13″) which is, however, twice as large as the observed extension. Thus, it may rather be due to the low sensitivity of the HST snapshot survey (600 s with the 2.4 m HST) compared to the groundbased image (1200 s with the 3.6 m ESO telescope).

In our long-slit observations, we detect [O III] emission at a $S/N > 3$ out to a distance of $r \sim 20″$ from the nucleus in both the south-east and north-west direction (Table 7). This is smaller than what has been reported by Bergeron et al. (1983), but they also find a decrease of line intensities by a factor of 10–30 at a distance >6″ from the nucleus and therefore average over a large spatial range to gain a constant $S/N$. The groundbased [O III] image of Morganti et al. (1998) also reveals a larger extension, but the HST [O III] extension is three times smaller. This discrepancy once again shows the need for alternative measures of the NLR size rather than using the [O III] extension alone.

Line ratios at a $S/N > 3$ can be measured out to a distance of $r \sim 13″$ from the photometric centre and all fall in the upper right corner in the three diagnostic diagrams (Fig. 4). Moreover, they show a remarkably small scatter compared to the AGN-typical line ratios of other galaxies, e.g. NGC 5643. We classify the corresponding gas as NLR, but we cannot exclude that the NLR extends even further out where we are not able to measure line ratios to a high accuracy.

In the centre, IC 5063 has the highest [O II]/Hβ flux ratio ($F_{dered} \sim 2.96$) and at the same time the lowest [O III]/Hβ ratio ($F_{dered} \sim 8.03$) of our sample (Table 4). This translates to the lowest ionisation parameter in the optical nucleus (Table 5). All values are indicative of a less strong ionisation field in the centre of IC 5063 compared to the other AGNs in our sample. The central electron temperature is with $T_{e,obs} \sim 13\,865 \pm 1800$ K comparable to that of other type 2s in our sample as well as to the central value measured by Colina et al. (1991) within the errors ($T_{e,obs} \sim 15\,000$ K). High excitation lines such as [Fe VII] and [Fe X] are observed in the central spectra.

IC 5063 is the only object in our sample where we can follow the [O III] λ4363 emission line at a $S/N > 3$ over several arcseconds from the nucleus (from ~8″ north-west to ~5″ south-east). The resulting temperature ranges between $T_{e,obs} \sim 15\,310$ K to $T_{e,obs} \sim 12\,245$ K, without a clear tendency with radius. The average value of the outer regions is with $T_{e,obs} \sim 13\,789 \pm 290$ K close to the central temperature of $T_{e,obs} \sim 13\,865 \pm 1800$ K. We cannot confirm the results of Bergeron et al. (1983) who reported an increasing temperature with distance from the nucleus, measured along a different PA (310° compared to our PA of 115°).

The central reddening determined from the Balmer decrement is the highest one found in our sample ($E_{B-V} \sim 0.89 \pm 0.01$ mag). It probably coincides with the red point source seen in NICMOS images of the nucleus of IC 5063 (Kulkarni et al. 1998). The reddening remains high 1″ northwest and decreases outwards (Fig. 3). In the south-east, it reaches a minimum at ~4″ and then increases again to a value comparable to the central one at a distance of 10″. This increase in the south-east is not observed in the reddening determined from the continuum slope relative to the stellar template (Fig. 3), indicating that it is most likely due to dust intrinsic to the NLR. Overall, both

reddening measures show a comparable reddening distribution, with the continuum slope reddening covering a smaller range of $\Delta E_{B-V} \sim 0.2$ mag, while the Balmer decrement yields a reddening distribution with an amplitude of $\Delta E_{B-V} \sim 1$ mag. We use the reddening determined from the H$\alpha$/H$\beta$ ratio to correct the observed line ratios.

The electron-density distribution peaks at the centre ($n_{e,obs} \sim 635 \pm 30$ cm$^{-3}$) and decreases outwards to the low density limit with two subpeaks at $\sim 5''$ on both sides of the optical nucleus. This general behaviour is similar to the results of Bergeron et al. (1983) and Colina et al. (1991) with a central electron density comparable to that of Bergeron et al. (1983) ($n_{e,obs} \sim 600$ cm$^{-3}$) and slightly higher compared to Colina et al. (1991) ($n_{e,obs} \sim 540$ cm$^{-3}$ without temperature correction versus their value of $n_{e,obs} \sim 450$ cm$^{-3}$ along a comparable PA of $\sim 110°$; their Fig. 9a).

IC 5063 is besides NGC 3281 the second object in our sample where the ionisation parameter does not peak at the optical nucleus. The highest ionisation is observed instead at $5''.5$ south-east of the nucleus. This increase towards the south-east is in agreement with the increasing ionisation parameter reported by Bergeron et al. (1983) and Colina et al. (1991), but towards the north-west, we observe a decreasing ionisation parameter. Interestingly, the position at which the ionisation parameter peaks is the same at which the surface-brightness distributions start to increase again outwards. Moreover, it coincides with the south-eastern region of enhanced electron density.

Colina et al. (1991) consider combined effects of abundance and density gradients as the most likely interpretation of these observations. However, the line ratios in all three diagnostic diagrams show a very small scatter, arguing against a steep abundance gradient. Moreover, the slope of decreasing electron density <2 needed to explain the increase in excitation conditions is not observed, neither in their data nor in our data ($n_{e,obs} \propto R^{-1.1}$; Table 9). We instead favour a shock scenario from the interaction of the radio jet and the NLR gas. This is strengthened by the close match between the radio map and the NLR as well as the blueshifted H I absorption and the broad profile of the H I absorption observed by Morganti et al. (1998). The shocks may result in a locally increased density and ionise the surrounding medium, resulting in the increased ionisation parameter and surface brightness. The shock scenario is supported by the emission-line profiles which show substructures in the central $9''$ with a blue asymmetry on the north-west side and a red asymmetry on the south-east side of the centre. The profiles get significantly broader especially $1$–$2''$ on both sides of the nucleus. Unfortunately, our observations are limited by spectral resolution to allow for a detailed discussion of profile variations. To probe the shock scenario, we looked for the presence of [Fe X] emission (e.g. Viagas-Aldrovandi & Contini 1989): It is negligible throughout most of the region, with the exception of the central $2''$ (centre: $F_{dered} \sim 0.02$, $1''$ north-west: $F_{dered} \sim 0.003$, $1''$ south-east: $F_{dered} \sim 0.001$, respectively) and at $3''$ south-east ($F_{dered} \sim 0.001$), i.e. close to the region where we observe an increased density. However, we are limited by both the signal and the low resolution which makes it difficult to disentangle the weak [Fe X] from [O I] $\lambda6363$ Å.

## A.2. NGC 7212

NGC 7212 is a Seyfert-2 galaxy in a system of three interacting galaxies (Wasilewski 1981). Line emission from ionised gas extending over $\sim 17''.5$ along both PA of $37°$ and $127°$ has been reported by Durret & Warin (1990) as observed by means of optical long-slit spectroscopy in the H$\beta$+[O III] wavelength range. They find a high excitation value $R = I([O III] \lambda5007$ Å$+4959$ Å$)/I(H\beta) = 19$ in the nucleus, while the nebulosity is of variable excitation with $R$ ranging from 5–28. They quote that the large values are uncertain as H$\beta$ is close to the detection limit.

Tran et al. (1992) find a broad H$\alpha$ component in the polarised light of NGC 7212. However, Tran (1995) argues that a significant amount of polarisation is probably not intrinsic to the nucleus of NGC 7212 but due to transmission through aligned dust grains in the host galaxy. This is supported by several observational evidences, showing that dust obscuration plays a significant role in the source. Moreover, the narrow permitted and forbidden lines also posses a substantial amount of polarisation.

Tran (1995) finds a jet-like high-ionisation feature extending up to $10''$ from the nucleus at a PA of $\sim 170°$ in ground-based [O III] and H$\alpha$ image, possibly due to collimated radiation of the nucleus. This direction coincides with a double radio source on a much smaller spatial scale discovered by Falcke et al. (1998) who compare HST and VLA observations of NGC 7212. The continuum image of Falcke et al. (1998) shows multiple dust lanes. The [O III] image exhibits extended emission out to $\sim 3''$ from the nucleus along PA = $170°$. The emission is diffuse and composed of several individual knots to the north and south of the nucleus.

Along a PA of $170°$, we observe [O III] emission extending out to $12''$ from the nucleus (Table 7), i.e. four times larger than the extension seen in the HST image in the same direction. It is somewhat smaller than the maximum extent observed by Durret & Warin (1990) (PA of $127°$ and $37°$). The excitation value we observe in the central spectrum is with $R_{obs} \sim 17$ comparable high to what has been observed by Durret & Warin (1990). It is the highest value in our type-2 sample. Note that the [O III]/H$\beta$ ratio given in Table 4 does not include the [O III] $\lambda4959$ Å line which is one third of the flux of the [O III] $\lambda5007$ Å line. Thus, one third of $F_{obs}$ given in Table 4 has to be added to gain $R$. The reddening-corrected value in the centre is $R_{dered} \sim 16$ and varies between 6 and 17 in the central $24''$ region, i.e. it stays high in the whole region which we classify as NLR. Emission-line ratios at a $S/N > 3$ were obtained out to $\sim 5''$ south-east of the nucleus and $\sim 10''$ north-west.

The reddening in the centre is rather low ($E_{B-V} = 0.33 \pm 0.01$ mag) and decreases to a value of $\sim 0.07$ mag at $1''$ north-west of the nucleus (Fig. 3). On both sides of this region, it increases and reaches its maximum value at $4''$ south-east and $7''$ north-west of the photometric centre ($\Delta E_{B-V} \sim 1$ mag). These maxima may be attributed to dust lines seen in the continuum image by Falcke et al. (1998).

The surface brightness is highest at $1''$ south-east of the centre (Fig. 5). Although the highest [O III] and H$\alpha$ flux as well as the highest continuum is observed at $0''$ (this is how we defined the photometric centre), the reddening-corrected luminosities peak at $1''$ south-east due to the higher reddening observed in this part. The surface-brightness distributions decrease outwards and show a secondary maximum at $\sim 6''$ north-west of the nucleus. In the same region, the highest $R_{dered}$ value of 17 is observed.

Both electron density and ionisation parameter show a slight increase at $\sim 8''$ north-west of the nucleus. As the radio maps of NGC 7212 show a double radio source extending in the direction of our long-slit observations (Falcke et al. 1998), it is probable that the radio jet interacts with the NLR, resulting in the

observed enhanced surface brightness, electron density, ionisation parameter, and the high excitation at ~6–8″ north-west of the nucleus.

### A.3. ESO 362-G008

Groundbased images of this Seyfert–2 galaxy were studied by Mulchaey et al. (1996), revealing a very red continuum nucleus. The [O III] emission is strongest in the nucleus and extends out to ~25″ along the galaxy disk (~158°, see Fig. 1) and ~10″ along the galactic minor axis. The regions of high excitation gas are distributed in a cross-like morphology, with the highest ratio corresponding to an off-nuclear cloud to the north-east. Colbert et al. (1996) interpret the presence of gas far out of the disk as sign of a large-scale outflow occurring in ESO 362-G008.

Fraquelli et al. (2000) studied the extended NLR of the Seyfert-2 galaxy ESO 362-G008 in detail to compare it to that of the Seyfert-1 galaxy MCG -05-13-017. They use a stellar population template obtained from averaging the extranuclear spectra. In the nucleus, a dilution of an intermediate-age burst of star formation is found. Fraquelli et al. (2000) find no evidence of a featureless continuum contributing more than 5% in the near-UV, in agreement with the results of Cid Fernandes et al. (2001). Emission-line fluxes are measured along PA = 60° out to 14″ from the nucleus. The H$\beta$ emission line is too weak to be measured, often not filling the absorption feature, indicating that the stellar template does not match the younger stellar population of the nuclear region. All ratios show a symmetric behaviour on both sides of the nucleus. The increasing [O II]/[O III] ratio indicates a decreasing ionisation parameter.

ESO 362-G008 is the only object in our sample in which strong underlying stellar absorption lines remain even after subtraction of a template determined in the outer parts of the galaxy (Table 3; Fig 2). This hints the existence of a nuclear starburst as is confirmed by the stellar population synthesis of Cid Fernandes et al. (1998) and the results of Storchi-Bergmann et al. (2000): They describe ESO 362-G008 as relatively evolved nuclear starburst due to its high order Balmer absorption lines. The continuum is very red due to a dust lane crossing the nuclear region as seen by Malkan et al. (1998) in broadband HST images.

As a consequence, our results have to be taken with some caution as the H$\beta$ and H$\alpha$ emission are most probably underestimated. We indeed often see the underlying absorption trough in both lines. Also Fraquelli et al. (2000) who use a stellar population template averaged from extranuclear spectra report dilution of an intermediate-age burst of star formation, resulting in a mismatch of the stellar template and the younger stellar population of the nuclear region where the H$\beta$ line is often not filling the absorption feature.

ESO 362-G008 is also the object in our sample with the smallest detectable [O III] extent ($r \sim 4''$). Moreover, due to the low *S/N*, the line ratio study is limited to the central $r \sim 3''$. Interestingly, the groundbased image reveals a more than twice as large [O III] extension (along roughly the same PA). Fraquelli et al. (2000) study emission lines out to $r \sim 14''$ from the nucleus but along PA = 60° and are also confined to the inner $d \sim 10''$ at a PA of 160°.

We decided not to apply more sophisticated stellar template corrections due to our limited *S/N*. All line ratios fall in the AGN regime in the diagnostic diagrams, suggesting that the NLR extends out to at least 3″ radius from the centre (Fig. 4). The line ratios have rather high values on the x-axis, most probably due to the underestimated H$\alpha$ line flux. Due to the remaining underlying absorption lines in the central spectra, only emission-line fluxes from the strongest lines [O II], H$\beta$, [O III], [O I], H$\alpha$, [N II], and [S II] can be derived (Table 4).

The reddening determined from the continuum slope relative to the template shows a similar distribution as the reddening distribution using the Balmer decrement with the highest reddening value in the centre and a slow decrease to the outer parts (Fig. 3). Note that the reddening of the continuum slope shown in Fig. 3 was set arbitrarily to zero for comparison. The reddening scatter derived from the continuum slope is small ($\Delta E_{B-V} \sim 0.07$ mag), while a ~10 times higher range is obtained using the H$\alpha$/H$\beta$ ratio ($\Delta E_{B-V} \sim 0.6$ mag). These differences can be explained first by the relative reddening value that was obtained in case of the continuum slope, i.e. both outer template and central spectra suffer similar dust extinction which do not reflect in the derived value. Second, dust may be intrinsic to the NLR. We used the reddening determined by the emission-line ratio for correction.

The decrease of the ionisation parameter we observe has already been suggested by Fraquelli et al. (2000) based on the increase of the [O II]/[O III] ratio, at least in the central $r \sim 5''$ (their Fig. 11).

### A.4. NGC 3281

Durret & Bergeron (1988) discovered the extended ionised envelope of $d \sim 21''$ in NGC 3281. They find a large reddening value of $E_{(B-V)} = 0.78$ mag in the nuclear region. The derived electron temperature equals to 28 000 K in the high excitation zone.

NGC 3281 has been classified as a proto-typical Seyfert-2 galaxy by Storchi-Bergmann et al. (1992) as it clearly shows features expected from the unified model: an ionisation cone, heavy obscuration towards the (hidden) nucleus, a wind outflow along the cone, and emission-line ratios consistent with photoionisation by a power-law continuum. They carried out the most extensive study of NGC 3281 including direct images in continuum, [O III], and H$\alpha$+[N II] as well as long-slit spectroscopy at several slit positions. The [O III] emission resembles the projection of a cone. The excitation map shows that either the reddening decreases from south to north or the excitation increases. The reddening distribution indicates that the nucleus is hidden by a dust lane. This is strengthened by nuclear spectra which show no dilution by a featureless continuum. The stellar population is old and typical of early-type galaxies. An S2 template from synthetic spectra by Bica (1988) was used to subtract the absorption lines and reddened to match several spectra which where heavily reddened. The stellar population seems not to vary much in the inner 22″ × 10″ region as suggested from the uniform equivalent width of absorption lines with the exception of Na I D. Storchi-Bergmann et al. (1992) interpret this observation by additional contribution to Na I D from interstellar absorption: Loci of higher Na I D equivalent widths correspond to regions with high $E_{(B-V)}$. The electron densities are found to be highest around the apex of the cone and decreasing with distance. The emission-line ratios are well described by photoionisation models with varying ionisation parameter. It seems that the ionisation parameter increases away from the apex along the axis of the cone, possibly due to a decrease of the density faster than $r^{-2}$.

The HST [O III] image resembles the groundbased one (Schmitt et al. 2003). It reveals a conically shaped NLR with opening angle of ~80° towards the north-east. The emission extends by 6.″1 towards the north-south direction and 3.″9 along the cone axis. Compared to the groundbased image, this extension is less than half the one measured by Storchi-Bergmann et al. (1992). This discrepancy is explained by Schmitt et al. (2003) by the limited field-of-view of the linear-ramp filter (~13″), but

can also be due to less sensitivity of the 800 s exposure taken with the 2.4 m HST mirror compared to the 900 s exposure using the 4 m CTIO telescope. The counter ionisation cone is mostly hidden by the host galaxy disk and only seen as a small blob of emission 4″.5 south of the nucleus. The [O III] emission is nearly perpendicular to the photometric major axis of the host galaxy (PA = 140°, RC3).

Vignali & Comastri (2002) study the broad-band X-ray spectrum of NGC 3281, revealing its Compton-thick nature. The nuclear continuum is heavily absorbed (column density $\sim 2 \times 10^{24}$ cm$^{-2}$).

In our longslit spectroscopy, the [O III] line emission at a $S/N > 3$ can be traced out to a distance of $r \sim 9''$ from the nucleus, i.e. three times as far as the maximum radius seen in the HST [O III] image of Schmitt et al. (2003). It is comparable to what has been found by Durret & Bergeron (1988) and Storchi-Bergmann et al. (1992). Line ratios with a $S/N > 3$ have been measured in the central $r \sim 5''$, showing values typical for AGN ionisation in all three diagnostic diagrams. Thus, the NLR extends out to at least $r \sim 5''$ from the optical nucleus.

The nuclear line intensity ratios relative to H$\beta$ are comparable to those of the other Seyfert-2 galaxies in our sample (Table 4). However, NGC 3281 has the lowest nuclear electron density of the type-2 sample ($n_{e,obs} \sim 540 \pm 40$ cm$^{-3}$; Table 5). In addition, the ionisation parameter determined in the nuclear spectrum is rather low. The central temperature is also the lowest observed with $T_{e,obs} \sim 13\,715 \pm 440$ K. This is significantly lower to what has been reported by Durret & Bergeron (1988) ($T_{e,obs} \sim 28\,000$ K).

The similarity in the reddening distribution we determined from the H$\alpha$/H$\beta$ line ratio as well as the continuum indicates that both the continuum and the emission lines are suffering extinction from foreground dust, e.g. the dust lane seen southwest of the nucleus (Storchi-Bergmann et al. 1992). The surface-brightness distributions fall smoothly with distance from the centre and show a secondary peak at 3″ north-east of the nucleus in the emission lines (Fig. 5). In the outer parts south-west of the photometric centre, the H$\alpha$ surface brightness approaches the value of [O III], indicating that the NLR may end somewhere close by. Unfortunately, we are limited by the $S/N$ to observe a transition towards H II regions. In Fig. 6, the electron-density distribution in NGC 3281 is shown. It peaks at the centre and decreases slowly outwards down to $n_{e,obs} \sim 110$–$240$ cm$^{-3}$, in agreement with the results of Storchi-Bergmann et al. (1992).

The ionisation parameter presented in Fig. 7 reaches the maximum value at 3″ north-east of the centre, coinciding with the secondary peak in the emission-line surface-brightness distribution. The increase towards the north-east is in agreement with the results of Storchi-Bergmann et al. (1992), but they also find an increase towards the south-west which we cannot confirm. It seems that this increase starts at a distance >5″ southwest from the nucleus where we do not trace the ionisation parameter any more due to limited signal. As the electron density does not drop off faster than $r^{-2}$ (neither in our observations nor in those of Storchi-Bergmann et al. 1992), this straightforward explanation of the observed increasing ionisation parameter with distance can be ruled out. Storchi-Bergmann et al. (1992) suggest that the gas near the apex of the cone where the reddening is large sees a partially obscured nuclear ionising source, resulting in a low ionisation parameter. Comparing CLOUDY photoionisation modelling with the observed emission-line ratios, they rule out shocks as primary ionisation mechanism. Moreover, no extended radio emission is observed which could hint the existence of radio jets (Schmitt 2001). Our observations do not help

to further elucidate the origin of the increased ionisation parameter towards the north-east.

We do not see double-peaked [O III] emission within the cone (i.e. from the centre towards the north-east), probably due to the low spectral resolution. Indeed, the profiles are very broad in the centre and out to $\sim 3''$ north-west.

### A.5. NGC 5643

The Seyfert-2 galaxy NGC 5643 is a barred spiral galaxy. It was studied in detail by Schmitt et al. (1994) by means of ground-based narrow-band imaging in [O III] and H$\alpha$+[N II] and long-slit spectroscopy. High excitation gas in a bi-conical morphology is elongated along the bar (PA = 90°) out to $\sim 16''$ on each side of the nucleus and out to $\sim 7''$ perpendicular. Further out, the H$\alpha$ image reveals several H II regions on both edges of the bar. Schmitt et al. (1994) speculate that the active nucleus is hidden $\sim 3''$ west of the continuum peak where both the highest reddening value and the highest gas density are observed. NGC 5643 is another Seyfert-2 galaxy fitting the unified model with the torus obscuring the nucleus and collimating the ionising radiation leading to the bi-conical morphology. In the central region, the stellar population is old corresponding to an S3 to S4 template, while in the H II regions, the stellar population is younger (S6-S7). Schmitt et al. (1994) did not use a stellar template to correct for the underlying absorption lines. Instead, only the H$\alpha$ and H$\beta$ lines were corrected using the corresponding equivalent widths. Dilution from a blue continuum probably due to scattered light is found in the inner 10″. The ratio [O III]/[O II] was used as tracer of the ionisation parameter. It is high throughout the extended NLR, decreasing more or less abruptly at its edges. Schmitt et al. (1994) found increasing oxygen (O) and nitrogen (N) abundances towards the centre where the O/H ratio reaches solar and N/H twice the solar value.

HST images in [O III] and H$\alpha$+[N II] were taken by Simpson et al. (1997) to study the NLR with a high-resolution of 0″.1 (Fig. 1). The one-sided conical distribution of the high-excitation gas is clearly seen. The peak of the red continuum emission coincides with the apex of the cone. The radio structure seen by Morris et al. (1985) is closely aligned with the overall shape of emission. A more detailed VLA A-array radio map (8.4 GHz) with radio structure closely matching the distribution of the NLR gas is presented by Leipski et al. (2006). It shows a diffuse radio jet extended by $\sim 15''$ to both sides of the centre (while in optical wavelength, the counter cone to the west is absorbed by dust).

Simpson et al. (1997) suggest that the absence of a visible counter cone is the consequence of its obscuration by the galaxy disk. An extended blue continuum region is seen out to 0″.9 east of the nucleus. It is not clear whether this emission is scattered nuclear continuum or due to e.g. a stellar ionising continuum.

NGC 5643 was included in the sample of 18 Seyfert galaxy studied by Fraquelli et al. (2003). They present density and reddening as a function of distance from the nucleus as well as surface-brightness distributions. However, their data have a significant lower signal-to-noise ratio ($S/N$) than our data and, moreover, they did not take into account the underlying absorption owing to the contribution of the stellar population which we show to be important.

We detect [O III] emission at a $S/N > 3$ out to a distance of $\pm 16''$ from the nucleus (Table 7), i.e. comparable to the results of Schmitt et al. (1994). However, only the central $\pm 11''$ originate from the NLR as can be seen in the first and third diagnostic diagram (Fig. 4). Further out, the emission originates from circumnuclear H II regions, in agreement with the results

of Tsvetanov & Petrosian (1995) who list 214 H II regions in NGC 5643, most of them distributed in a ring-like structure at 20–60″ from the nucleus, suggesting that current star formation is occurring in the nearly circular spiral arms. At a PA of 90° along the bar, the nearest H II regions are seen ~10″ east of the nucleus. Indeed, we observe a transition between line ratios typical for AGN ionisation and H II-region like ionisation occurring at a distance of 11″ from the centre, thus determining the size of the NLR to 11″ (≃ 1050 pc). This size coincides with the region in which Schmitt et al. (1994) report dilution from a blue continuum. While Fraquelli et al. (2003) detect line emission which they classify as extended NLR out to a distance of ~15–20″, our analysis shows that the extended emission beyond 11″ originate from circumnuclear H II regions and can therefore not be attributed to the NLR. In addition to the central [O III] emission, line-emission is found at distances of $47 \pm 3$″ west from the centre as well as $36 \pm 5$″ east and again $73 \pm 2$″ east from the photometric centre, attributable to H II regions identified by Tsvetanov & Petrosian (1995) and Schmitt et al. (1994). This is strengthened by the line ratios which all fall in the H II-region regime in the diagnostic diagrams (open and filled diamonds in Fig. 4). When comparing the line ratios of these H II regions with those of the circumnuclear H II regions, it is notable, that the ones from the centre (out to 16″ east) slowly approaches the outer ones in terms of the [O III]/H$\beta$ ratio. It shows that the transition between NLR and circumnuclear H II regions is not abrupt but that the dominating ionisation field slowly changes from the central AGN to that of the circumnuclear stellar one. At 16″ east (marked with the small letter "p" in Fig. 4), the line ratios are finally identically with those observed in the H II regions in the spiral arms. This observation strengthens our interpretation of the observed transition as true border between NLR and surrounding H II regions.

The reddening is highest in the centre and falls quickly towards the east and also 2″ to the west where it then again rises and stays high throughout the western NLR (Fig. 3). The high reddening in the west may originate from obscuration of dust lanes seen in broadband NICMOS/WFPC colour maps (Simpson et al. 1997; Quillen et al. 1999). The obscuration from dust seems to be responsible for the one-sided ionisation cone structure seen in the HST images of Simpson et al. (1997). Schmitt et al. (1994) observe the highest reddening at 3″ west of the continuum peak and speculate that the AGN is hidden there while we observe the highest reddening value in the centre. However, one has to take into account their spatial resolution of 2″ compared to our spatial resolution of ~1″. Moreover, the coincidence of the highest reddening with the most luminous spectrum (continuum, H$\alpha$ and [O III]) we find is in agreement with the schematic model proposed by (Simpson et al. 1997, their Fig. 6).

The electron density is slightly higher 1″ west of the photometric centre than in the centre itself. Schmitt et al. (1994) also report the highest density at 1″8 west of the nucleus (their first data point west of the photometric centre). The AGN may indeed reside slightly offset to the west of the [O III] and H$\alpha$ peak as suggested by Simpson et al. (1997).

Due to the fairly high spectral resolution of the NTT data taken by Christian Leipski (~1.5 Å ≃ 90 km s$^{-1}$), we are able to study the emission-line profiles in detail (Fig. A.1). Interestingly, the velocity field is reflected in the profiles of H$\beta$, [O III], and H$\alpha$: At the location of the redshifted velocities to the east of
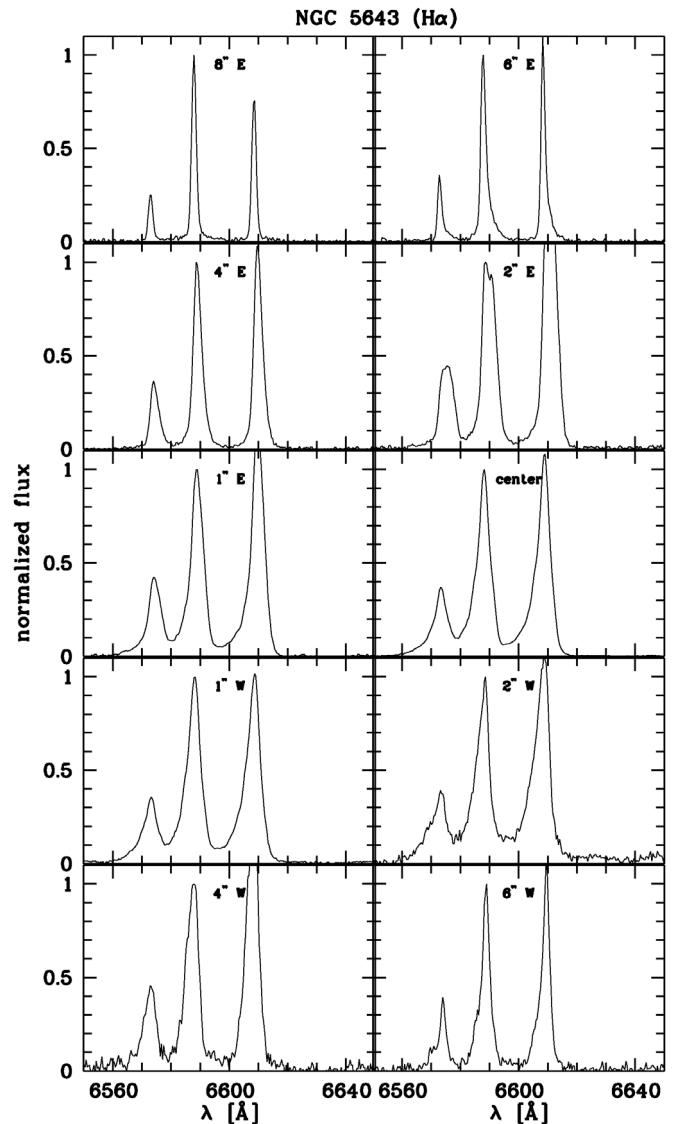


**Fig. A.1.** H$\alpha$ profile variations in NGC 5643. The peak flux of H$\alpha$ is normalised to 1.

the nucleus, we see red wings in the profiles out to ~8″. The strongest red contribution leading even to a secondary peak is observed at 2″ east of the nucleus, i.e. coinciding with the region where the highest velocity occurs. From 1″ east of the nucleus out to ~7″ west of the nucleus, a blue wing is observed which reaches its maximum contribution to the total flux at ~3–4″ west of the nucleus, i.e. coinciding with the maximum blueshifted velocity. Along with the profile asymmetries, the observed profiles get also broader. Whittle (1982) already reported that the line profiles are identical within observational uncertainties across the nuclear region and reveal profile asymmetries such as blue wings. The pronounced profile substructure is confined to the NLR, i.e. the central 22″ as determined from the diagnostic diagrams. The observed profile substructure may also reflect the influence of the bar potential. However, we cannot rule out that both the observed profile substructure and the red- and blueshifted velocities originate from outflowing gas due to jet/NLR interactions: Two radio lobes extend in the direction of the bar (Morris et al. 1985).